



RESEARCH ARTICLE

10.1029/2020MS002418

Key Points:

- Two baseline examples of fully coupled CESM with idealized ocean geometry capture many features of Earth's circulation
- The nominally ocean-covered coupled model has a global cold belt of equatorial upwelling and corresponding "reverse Hadley" cells
- The addition of a pole-to-pole strip continent leads to zonal asymmetry that makes the model's circulation more Pacific-like

Supporting Information:

Supporting Information may be found in the online version of this article.

Correspondence to:

X. Wu,
xiaoning.wu.1@stonybrook.edu

Citation:

Wu, X., Reed, K. A., Wolfe, C. L. P., Marques, G. M., Bachman, S. D., & Bryan, F. O. (2021). Coupled aqua and ridge planets in the community earth system model. *Journal of Advances in Modeling Earth Systems*, 13, e2020MS002418. <https://doi.org/10.1029/2020MS002418>

Received 24 NOV 2020

Accepted 1 APR 2021

Coupled Aqua and Ridge Planets in the Community Earth System Model

Xiaoning Wu¹ , Kevin A. Reed¹ , Christopher L. P. Wolfe¹ , Gustavo M. Marques² , Scott D. Bachman² , and Frank O. Bryan²

¹School of Marine and Atmospheric Sciences, Stony Brook University, Stony Brook, NY, USA, ²Climate and Global Dynamics Laboratory, National Center for Atmospheric Research, Boulder, CO, USA

Abstract Idealized models can reveal insights into Earth's climate system by reducing its complexities. However, their potential is undermined by the scarcity of fully coupled idealized models with components comparable to contemporary, comprehensive Earth System Models. To fill this gap, we compare and contrast the climates of two idealized planets which build on the Simpler Models initiative of the Community Earth System Model (CESM). Using the fully coupled CESM, the Aqua configuration is ocean-covered except for two polar land caps, and the Ridge configuration has an additional pole-to-pole grid-cell-wide continent. Contrary to most sea surface temperature profiles assumed for atmosphere-only aquaplanet experiments with the thermal maximum on the equator, the coupled Aqua configuration is characterized by a global cold belt of wind-driven equatorial upwelling, analogous to the eastern Pacific cold tongue. The presence of the meridional boundary on Ridge introduces zonal asymmetry in thermal and circulation features, similar to the contrast between western and eastern Pacific. This zonal asymmetry leads to a distinct climate state from Aqua, cooled by $\sim 2^{\circ}\text{C}$ via the radiative feedback of clouds and water vapor. The meridional boundary of Ridge is also crucial for producing a more Earth-like climate state compared to Aqua, including features of atmospheric and ocean circulation, the seasonal cycle of the Intertropical Convergence Zone, and the meridional heat transport. The mean climates of these two basic configurations provide a baseline for exploring other idealized ocean geometries, and their application for investigating various features and scale interactions in the coupled climate system.

Plain Language Summary Simplified climate models can improve our understanding of the Earth's climate system by stripping down its complexities. For example, atmospheric scientists often use idealized models with fixed sea surface temperature that is uniform in the east-west direction. Meanwhile, oceanographers often use box-shaped models driven by fixed wind. Although simplified models with full atmosphere-ocean interactions are few, previous studies have shed light on fundamental processes governing Earth's climate, including the poleward transport of energy. However, the coarse "pixel size" and overly reduced components are hard to relate to contemporary models for international climate assessments. To bridge this gap, we present two simplified models within components and resolution similar to that of state-of-the-art climate models. The nominally ocean-covered model, without continents blocking the east-west direction, develops a global cold belt of upwelling around the equator. In contrast, the model with an additional pole-to-pole strip continent is more Pacific-like with a western pool and eastern cold tongue. While broadly consistent with previous works, these new models show more details in the tropical region that affect the Hadley cells and rainfall. The capability of these simplified models is promising for addressing atmosphere-ocean interactions of scientific and societal interests, such as El Niño and hurricanes.

1. Introduction

Idealized models are illuminating tools for understanding Earth's climate system (Held, 2005; Maher et al., 2019). They reduce the complexities of the coupled climate system by simplifying the model design, such as ocean geometry, model forcing, or physical parameterization (e.g., Farneti & Vallis, 2009; Medeiros et al., 2016). Through these simplifications, idealized models have helped advance the scientific understanding of various aspects and scales of the climate system (e.g., Abernathay et al., 2013; Brunetti et al., 2019; Chavas et al., 2017; Ferreira et al., 2010; Manabe & Bryan, 1969; Voigt & Shaw, 2015; Wolfe & Cessi, 2010). They are also useful for the evaluation and development of climate model components

(Bachman & Fox-Kemper, 2013; Chang et al., 2001; Herrington & Reed, 2017; Jansen et al., 2019; Reed & Jablonowski, 2012). In the modeling community, it has been suggested that the utility of idealized models is best realized within a hierarchy of complexity leading up to state-of-the-art, comprehensive Earth System Models (Jeevanjee et al., 2017; Polvani et al., 2017), including those used for climate projection and assessments (Eyring et al., 2016). The availability of idealized models within such a hierarchy can serve as a valuable resource for climate research and education (e.g., Schultz et al., 2017).

Focusing on the atmosphere-ocean system, ocean-covered representations of Earth (commonly referred to as aquaplanets) have been widely used for either the atmospheric or ocean component at various degree of complexity, but fully coupled configurations are relatively scarce. For the atmospheric component, there is a rich history of application for aquaplanets (Blackburn et al., 2013; Neale & Hoskins, 2000), with either prescribed sea surface temperature (e.g., Medeiros et al., 2016) or slab ocean configurations (e.g., Benedict et al., 2017; Donohoe et al., 2014; Zhang et al., 2016) as the simplified lower boundary condition, forgoing ocean dynamics. Example topics of study using aquaplanet configurations include the hemispheric asymmetry in tropical rainfall (Frierson et al., 2013), the length scale of extratropical storm tracks (Kaspi & Schneider, 2011), and the effect of off-equatorial thermal forcing on tropical cyclone activity (Ballinger et al., 2015). For the ocean component, idealized ocean basins forced by a prescribed atmosphere are used for understanding the overturning circulation (Cessi & Jones, 2017; Ferrari et al., 2017; Johnson et al., 2019; Jones & Cessi, 2016; Nadeau & Jansen, 2020; Wolfe & Cessi, 2010), abyssal circulation (Jansen & Nadeau, 2016; Nadeau et al., 2019), and factors affecting salinity (Jones & Cessi, 2017, 2018). These studies demonstrate a wide range of key processes in the climate system where idealized models facilitate their interpretation with theory, guiding the understanding of more complex models.

For global and coupled configurations, earlier works (Farneti & Vallis, 2009; Smith et al., 2006) have explored the global climates of selected ocean geometries. Other notable examples using coupled aquaplanets include a hierarchy of idealized ocean geometries (Enderton & Marshall, 2009; Ferreira et al., 2010; Marshall et al., 2007). These simplified designs demonstrate remarkable resemblance to the observed Earth climate on the planetary scale, including the meridional heat transport (Czaja & Marshall, 2006; Enderton & Marshall, 2009; Marshall et al., 2007) and ocean salinity contrast (Ferreira et al., 2010; Nilsson et al., 2013). However, these configurations, oriented toward the global-scale ocean circulation with extremely simplified atmospheres (e.g., Molteni, 2003) at $\sim 3^\circ$ horizontal resolution or coarser, do not aim to address important atmospheric processes that depend on higher horizontal and vertical resolution, or more complete model physics (Ballinger et al., 2015; Herrington & Reed, 2017).

In summary, the gap in the hierarchy between previously available idealized models and comprehensive Earth System Models leads to missed opportunities in enhancing our understanding of fundamental climate dynamics with increasingly advanced modeling developments. Comprehensive models—such as those used for the Coupled Model Intercomparison Project (CMIP; Eyring et al., 2016)—have progressed to capture an increasing range of climate variability, extremes, and their associated impacts; however, the complexity of these models can complicate our understanding of these phenomena and the model dynamics driving them (e.g., Emanuel, 2020; Jeevanjee et al., 2017). Whereas simplified models can aid our theoretical and conceptual understanding, there is currently no coupled idealized model available with CMIP-equivalent comprehensive model physics for both the atmospheric and oceanic components. This lack of availability impedes the process-level understanding of CMIP-class models where atmosphere-ocean coupling plays a key role, and complicates the investigation of coupled phenomena of scientific and societal interest (e.g., Carranza et al., 2018; Li & Srivastava, 2018; Scoccimarro et al., 2017).

To fill this gap, by building on the Simpler Models initiative (Polvani et al., 2017, <http://www.cesm.ucar.edu/models/simpler-models>) of the Community Earth System Model (CESM; Danabasoglu et al., 2020; Hurrell et al., 2013), we have developed two fully coupled baseline configurations with idealized ocean geometry. The new development brings unique, CMIP-relevant modeling capabilities into the idealized framework. In this study, we present the mean climates of the two configurations and discuss the contrast between them. The first one, Aqua, is ocean-covered except for minimal polar land caps; the second one, Ridge, has a single meridional boundary. The selection of these two geometries is motivated by their simplicity and elegance. They are simple as first-order idealizations of the Earth commonly adapted by the atmospheric and oceanographic communities, respectively. They are also elegant for capturing a range of realistic Earth features

on the global scale, as suggested by previous works (Enderton & Marshall, 2009; Smith et al., 2006) and shown in Section 3: Aqua presents Southern Ocean characteristics, while Ridge is a striking analog of the Pacific. Comparing and contrasting with previous idealized studies, these two configurations demonstrate the role of ocean geometry in the coupled climate state, including impacts on meridional heat transport. The evaluation of these two basic configurations serves as the foundation for additional forms of idealized ocean geometries, and their application to investigating various phenomena and processes in the coupled climate system.

This paper is organized as follows. Section 2 describes the details of model configuration, and the simulation data under analysis. Section 3 presents the mean climates of the CESM Aqua and Ridge planets from the perspectives of the energy budget, the large-scale circulation, and the meridional heat transport. Finally, Section 4 discusses the results in the context of previously documented models and the outlooks for future work.

2. Data and Methods

The idealized configurations are developed in the framework of CESM (Danabasoglu et al., 2020; Hurrell et al., 2013), a state-of-the-art, community modeling tool. With numerous options for configuration and a vibrant user community, CESM provides the capability to produce simulations for international climate assessments (Eyring et al., 2016), as well as reduced-complexity options for fundamental investigations and continued model component development (Polvani et al., 2017). We expand on currently available options of atmosphere-only or slab ocean aquaplanets (Benedict et al., 2017; Medeiros et al., 2016), and introduce fully coupled configurations with dynamical oceans.

Two types of idealized ocean geometries are configured, as shown in Figure 1. For Aqua, the planet is ocean-covered except for two polar continents that reach down to 80°N/S. The presence of the polar continents, occupying minimal area, is required by the ocean grid. For Ridge (Enderton & Marshall, 2009; Smith et al., 2006), a single grid-cell-wide strip of pole-to-pole continent is added as a meridional boundary for the ocean basin. All land has zero orography.

The atmospheric component is the Community Atmosphere Model version 4 (CAM4; Neale et al., 2010). The choice of model version is made to balance complexity and computational cost. The finite-volume dynamical core, based on a regular latitude-longitude grid, is built upon a 2D shallow water approach (Lin & Rood, 1996, 1997) and mass-conservative in flux-form. The parameterization schemes include deep convection (Zhang & McFarlane, 1995), shallow moist convection (Hack, 1994), dry boundary layer turbulence (Holtslag & Boville, 1993), and cloud physics, radiation, etc. further described in Neale et al. (2010). The horizontal resolution is nominally 1°, resulting in grid spacing of ~110 km in the tropical regions. In the vertical direction, the model is divided into 26 layers in a hybrid sigma-pressure coordinate system, with finer spacing near model bottom and top (~3 hPa). Settings for the solar constant, dry mass, greenhouse gas concentrations, ozone distribution, and aerosols are adapted from the Aqua-Planet Experiment (Neale & Hoskins, 2000).

The ocean component is the Modular Ocean Model version 6 (MOM6; Adcroft et al., 2019), which will replace the previous ocean component for CESM3. One advantage of MOM6 is the versatile specification of vertical layers via the use of the Arbitrary-Lagrangian-Eulerian algorithm (Bleck, 1978; Hirt et al., 1974). The horizontal resolution is nominally 2°, with equatorial refinement to 1°. The equatorial refinement allows for adequate representation of tropical instability waves, and—with similar grid spacing as the atmosphere—captures the gradients of wind stress. The ocean maximum depth is 4,000 m, divided into 57 vertical layers, with thickness decreasing from ~250 m at the bottom to 2.5 m near the ocean surface. The effects of mesoscale eddies are parameterized by activating two schemes in the tracer equation. The first scheme follows the ideas of Gent et al. (1995), where available potential energy is removed from the large scale by flattening isopycnals. A constant thickness diffusivity of $2,000 \text{ m}^2 \text{ s}^{-1}$ is used without any vertical structure. The associated eddy-induced transport is applied as a bolus velocity. To avoid the problems associated with layer thickness diffusion described by Holloway (1997), this scheme is implemented as an interface height diffusion. Following Solomon (1971) and Redi (1982), the second scheme represents the diffusive mixing of tracers along neutral surfaces, which is implemented using a finite-volume general-coordinate

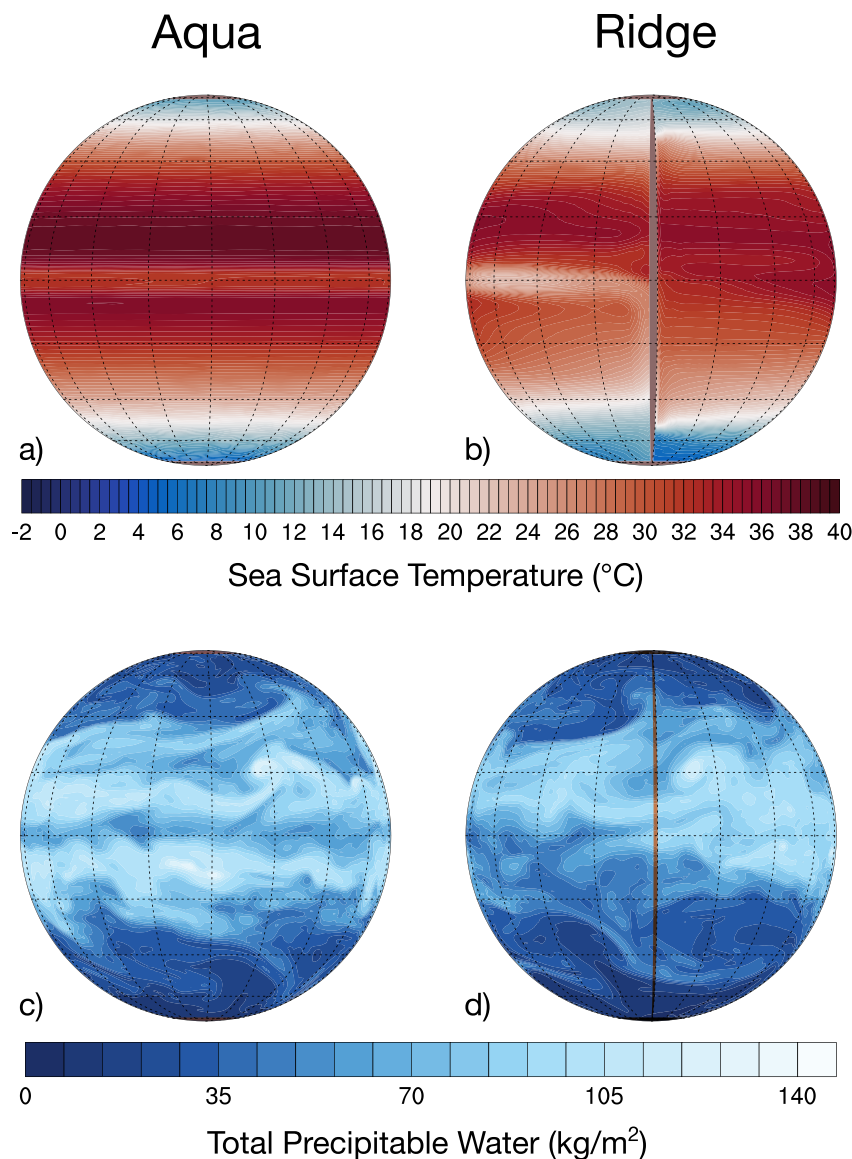


Figure 1. Illustration of the Aqua and Ridge planets. The polar land caps and the ridge continent are marked in brown. (a–b) SST ($^{\circ}$ C) for August (100-years climatology), showing the global cold belt of equatorial upwelling on Aqua, and the eastern and western boundary currents on Ridge (see animation of the seasonal cycle in supplement). (c–d) Instantaneous snapshots of total precipitable water (kg m^{-2}) from boreal summer, displaying various synoptic systems.

methodology (Shao et al., 2020). Again, a constant along-isopycnal tracer diffusivity of $2,000 \text{ m}^2 \text{ s}^{-1}$ is used. The K-Profile vertical mixing Parameterization (KPP; Large et al., 1994) is applied via the Community ocean Vertical Mixing (CVMix; Griffies et al., 2015) framework. The diapycnal diffusivity is $2 \times 10^{-5} \text{ m}^2 \text{ s}^{-1}$, the Laplacian horizontal viscosity is $1 \times 10^4 \text{ m}^2 \text{ s}^{-1}$, and the coefficient for quadratic bottom drag is 0.005. To provide topographic form drag for balancing the momentum input from the atmosphere, we prescribe zonally and hemispherically symmetric bottom topography in analytical, sinusoidal form (see Figure S1). The topographic form drag is particularly important for the Aqua case, and we use the same bottom topography in both cases for consistency. The bottom topography has the maximum height of 500 m in the vertical, with horizontal length scale of 1,000 km in the meridional direction, and 45° in the zonal direction. The height is chosen to be on the scale of—but slightly larger than—the thickness of bottom layers, and the horizontal length scales are chosen to avoid subgrid-scale signals (cf. comparable design of bottom topography in Jansen et al., 2019).

Table 1
Statistics of the Global Mean, Annually Averaged Over Year 401–500

| | Unit | Aqua | | Ridge | |
|--------------------------------------|----------------------|----------|--------|----------|--------|
| | | Avg. | Stdev. | Avg. | Stdev. |
| Surface temperature | °C | 27.466 | 0.104 | 25.503 | 0.071 |
| Surface pressure | hPa | 1016.580 | 0.067 | 1015.690 | 0.040 |
| Total cloud fraction | fraction | 0.444 | 0.002 | 0.472 | 0.004 |
| Cloud radiative forcing | W m ⁻² | -23.166 | 0.250 | -25.857 | 0.315 |
| Total precipitable water | kg m ⁻² | 58.070 | 0.694 | 49.194 | 0.396 |
| Precipitation rate | mm day ⁻¹ | 4.384 | 0.020 | 4.182 | 0.014 |
| Net shortwave (TOA) | W m ⁻² | 261.507 | 0.223 | 257.822 | 0.345 |
| Net longwave (TOA) | W m ⁻² | 261.129 | 0.286 | 258.091 | 0.236 |
| Net shortwave (ocean surface) | W m ⁻² | 183.856 | 0.318 | 181.852 | 0.390 |
| Net longwave (ocean surface) | W m ⁻² | -44.443 | 0.378 | -48.341 | 0.252 |
| Downwelling longwave (ocean surface) | W m ⁻² | 424.391 | 1.057 | 408.145 | 0.644 |
| Latent (ocean surface) | W m ⁻² | -129.284 | 0.586 | -123.159 | 0.387 |
| Sensible (ocean surface) | W m ⁻² | -9.683 | 0.107 | -10.578 | 0.092 |
| Ocean potential temperature | °C | 8.566 | 0.015 | 7.553 | 0.026 |

Note. Global mean ocean salinity is a constant value of 34.969 psu for both planets, due to the absence of sea ice.

The sea ice component is the Community Ice CodE version 5 (CICE5; Bailey et al., 2018), with full thermodynamics and dynamics. Since the quasi-equilibrium climate states of both configurations are too warm for sea ice formation (see Table 1), the sea ice component is present but not active for the period under analysis in the present study. As needed by the minimal presence of land, the land component is the Community Land Model version 5 (CLM5; Lawrence et al., 2019) at the same horizontal resolution as the atmospheric component. For the polar and ridge continents, the land surface type is set to wetland, which behaves most similarly to a slab ocean in comparison with other land surface types. Precipitation over land, a small amount, is returned to the ocean by adjusting the water balance in the MOM6 component. The coupling is handled by the Common Infrastructure for Modeling the Earth (CIME; <http://github.com/ESMCI/cime>, see description in Danabasoglu et al., 2020). The coupling frequency for all components is hourly, based on the spatial resolution of model components.

For both Aqua and Ridge configurations, the diurnal cycle is retained, and an idealized seasonal cycle is imposed by setting the orbital obliquity to 23.3°. Model initialization is zonally symmetric for all components (atmosphere, ocean, land, and sea ice). On the National Science Foundation (NSF)-supported Cheyenne supercomputer housed at the National Center for Atmospheric Research (NCAR), the model achieves throughput of ~80 simulated years per wall-clock day, while archiving annually averaged output for the ocean and monthly averaged output for all other components. By Year 400 of the 500-yr integration, although the deep ocean is still drifting, the top-of-atmosphere (TOA) radiative balance has adjusted close to equilibrium for both configurations (imbalance $\sim O(0.1)$ W m⁻², see Table 1 and Figure S2). We discuss the climate state of Year 401–500 in the following section, using monthly averaged output for the atmosphere and annually averaged output for the ocean.

3. Results

Figure 1 illustrates the state of the coupled Aqua and Ridge planets, with snapshots of their oceans and atmospheres in boreal summer. Both planets are warm and ice-free. For the zonally symmetric Aqua, the sea surface temperature (SST; Figure 1a) shows a global cold belt of equatorial upwelling that persists through the seasonal cycle (see animation in supplement). A common feature of coupled Aqua configurations with dynamical oceans (Farneti & Vallis, 2009; Marshall et al., 2007; Smith et al., 2006), this local SST minimum

on the equator is markedly different from the typical SST patterns used for atmosphere-only Aqua-Planet Experiments (Neale & Hoskins, 2000). For Ridge (Figure 1b), the presence of the meridional boundary leads to the formation of a western warm pool, limiting the global equatorial upwelling of Aqua to eastern upwelling in the cold tongue. Analogous to the Pacific, besides the local equatorial upwelling, the equatorward eastern boundary current also contributes to the cold tongue via advection (Kessler, 2006; Wyrtki, 1981). These SST patterns, in turn, influence the characteristics of their atmospheres. Both planets exhibit a rich variety of synoptic systems, including extratropical storms and tropical cyclone-like vortices (Figures 1c and 1d). For Aqua (Figure 1c), on either side of the cold and dry equator, the atmosphere is remarkably rich in moisture even in the winter hemisphere. This is associated with Aqua's unique circulation patterns in the seasonal cycle, discussed later in Section 3.2. For Ridge (Figure 1d), the winter hemisphere is noticeably drier compared to its summer hemisphere, especially around the cold tongue and the eastern boundary current. The presence of the western warm pool is reflected in the rich reservoir of atmospheric moisture in the region.

The contrast in these thermodynamic and dynamic features, with an emphasis on the zonal asymmetry of Ridge, is further detailed in Figure 2 with the 100-years climatology. For Aqua (Figure 2, left column), the equatorial atmosphere is uniformly associated with subsidence (Figure 2a), as a result of local SST minimum in the equatorial region. Driven by mild easterly wind stress (Figure 2c), the equatorial belt of upwelling (Figure 2e) produces a shallow thermocline in the ocean underneath (Figure 2i). In contrast, Ridge (Figure 2, right column) produces many Pacific-like features (cf. Ch. 11 in Gill, 1982, on the correspondence between surface heating and zonal mass flux of the Walker circulation): a Walker-like circulation (Figure 2b) develops, with convection over the moist western warm pool, and subsidence over the dry eastern cold tongue; the convergence of zonal wind stress around 120°E (Figure 2d) marks the location of the warmest equatorial SST (Figure 2f), producing a zonal SST gradient of ~8°C averaged over 5°N–5°S (Figure 2h), contrary to Aqua's zonal uniformity (Figure 2g). Correspondingly, the equatorial thermocline (Figure 2j) deepens from the eastern end: the 18°C isotherm deepens all the way to ~300 m at the western boundary, whereas the 28°C isotherm reaches maximum depth in the middle of the ocean basin before shoaling again in the west. The western warm pool is established at a distance away from the western boundary (~1/3 of the basin width).

The fundamental role of the meridional ocean boundary in determining the global climate, as suggested by Figures 1 and 2, are further analyzed in the subsections below. Contrasting the climates of Aqua and Ridge, we explore the following aspects: the global energy budget, the large-scale circulation with seasonality, and the resulting meridional heat transport.

3.1. Global Energy Budget and Balance

The differences between the global mean climates of Aqua and Ridge are presented in Table 1, which summarizes the statistics of global mean values concerning the energy budget and the water cycle over the annually averaged 100-year period under analysis. In virtually all aspects, the differences between the global mean state of Aqua and Ridge are well beyond the range of their respective interannual variability, as measured by the standard deviation of the global mean.

The warmth of the climate states—with ~27°C global mean surface temperature for Aqua—are comparable to Smith et al. (2006), although greater contrast between Aqua and Ridge is presented here. Aqua is ~2°C warmer in global mean surface temperature and ~1°C warmer in global mean ocean potential temperature compared to Ridge (Table 1). In the energy budget, this corresponds to greater net shortwave heating at the top-of-atmosphere (TOA), as well as at the ocean surface. The radiative forcing of clouds plays a large role in the cooling of Ridge relative to Aqua: the prominent cloud radiative cooling in the tropics, due to the presence of the western warm pool on Ridge with its convective activities, is reflected in the global mean.

The meridional structure of the energy budget is further detailed in Figure 3. In the zonal average of the TOA radiative budget (Figures 3a–3d), both Aqua and Ridge qualitatively resemble Earth observations (e.g., Stephens et al., 2015). The extent of the tropics is essentially identical for both planets, with poleward limits at 37.2°N/S as defined by TOA radiative surplus. In the zonal average, the net tropical heating of Aqua is greater relative to Ridge at both TOA and the ocean surface. At TOA, Aqua receives more shortwave

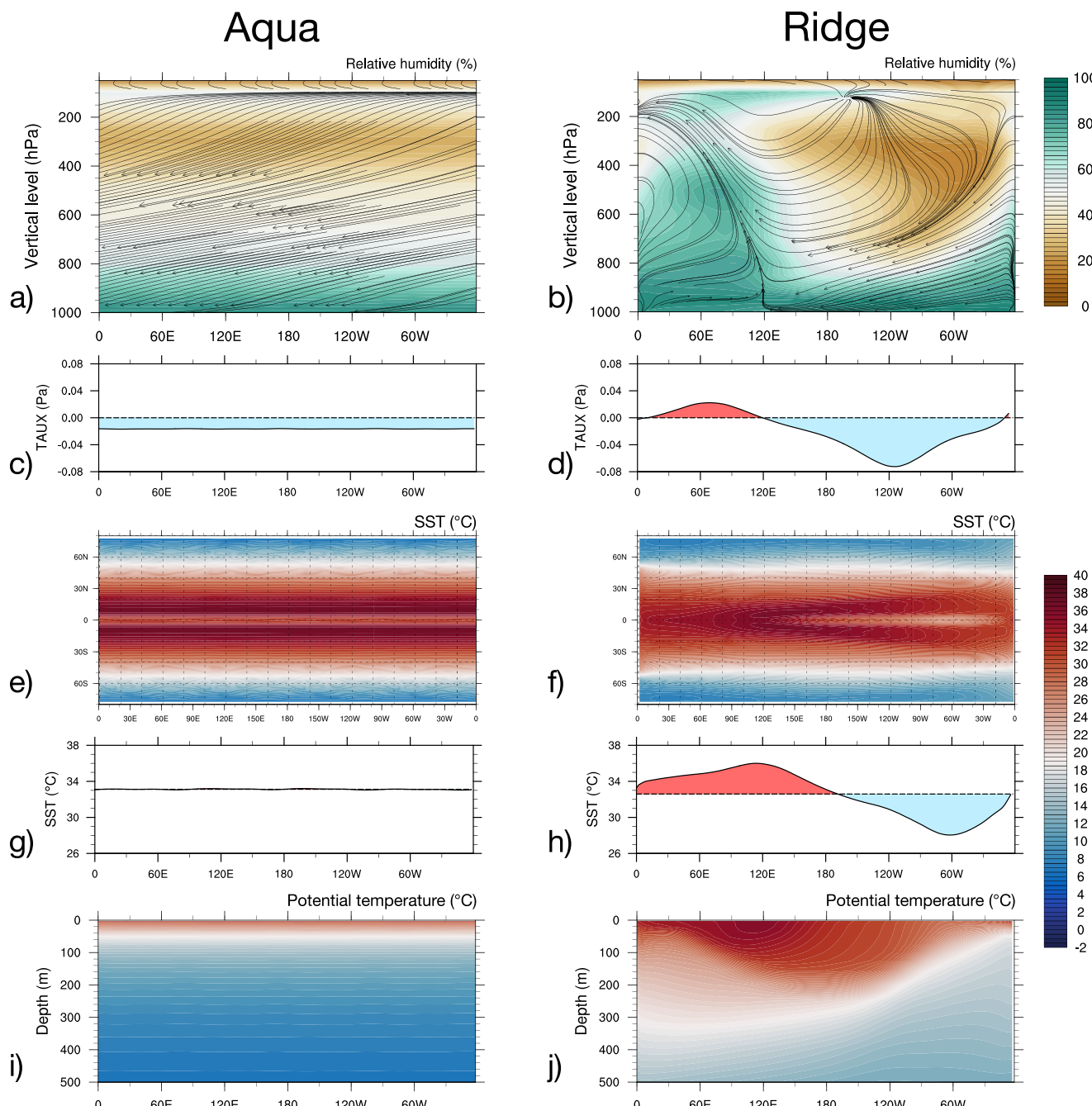


Figure 2. Zonal features in the tropics, 100-years climatology. (a–b) Zonal circulation in the atmosphere with Walker-like feature on Ridge, seen in relative humidity (colored shading), and streamline of zonal and vertical velocity (solid arrows). Vertical velocity is scaled by a factor of 50 for visualization. (c–d) Zonal gradient of zonal wind stress (Pa), the dashed horizontal line marking 0; (e–f) SST (°C). (g–h) Zonal gradient of SST (°C), the dashed horizontal line marking the zonal average value. (i–j) Equatorial thermocline, as seen in potential temperature (°C). All panels except for (e–f) are averaged 5°N–5°S.

(Figures 3a and 3b) and integrated net surplus heating (Figures 3c and 3d) than Ridge. Over the ocean surface (Figures 3e and 3f; cf. qualitative similar decomposition in Earth observations, Ch. 5 in Talley, 2011), the heating of Aqua relative to Ridge in the deep tropics is mostly due to greater net shortwave and lesser latent heat loss over the equatorial cold belt (see Figure S3). Specifically, the presence of the western warm pool on Ridge (Figure 2, right column) reduces surface shortwave flux via cloud forcing, and enhances latent heat loss of the ocean by greater evaporation associated with its warmer temperature. These effects are analogous to observed surface heat fluxes in the Pacific (e.g., Grist & Josey, 2003), where the Eastern Pacific

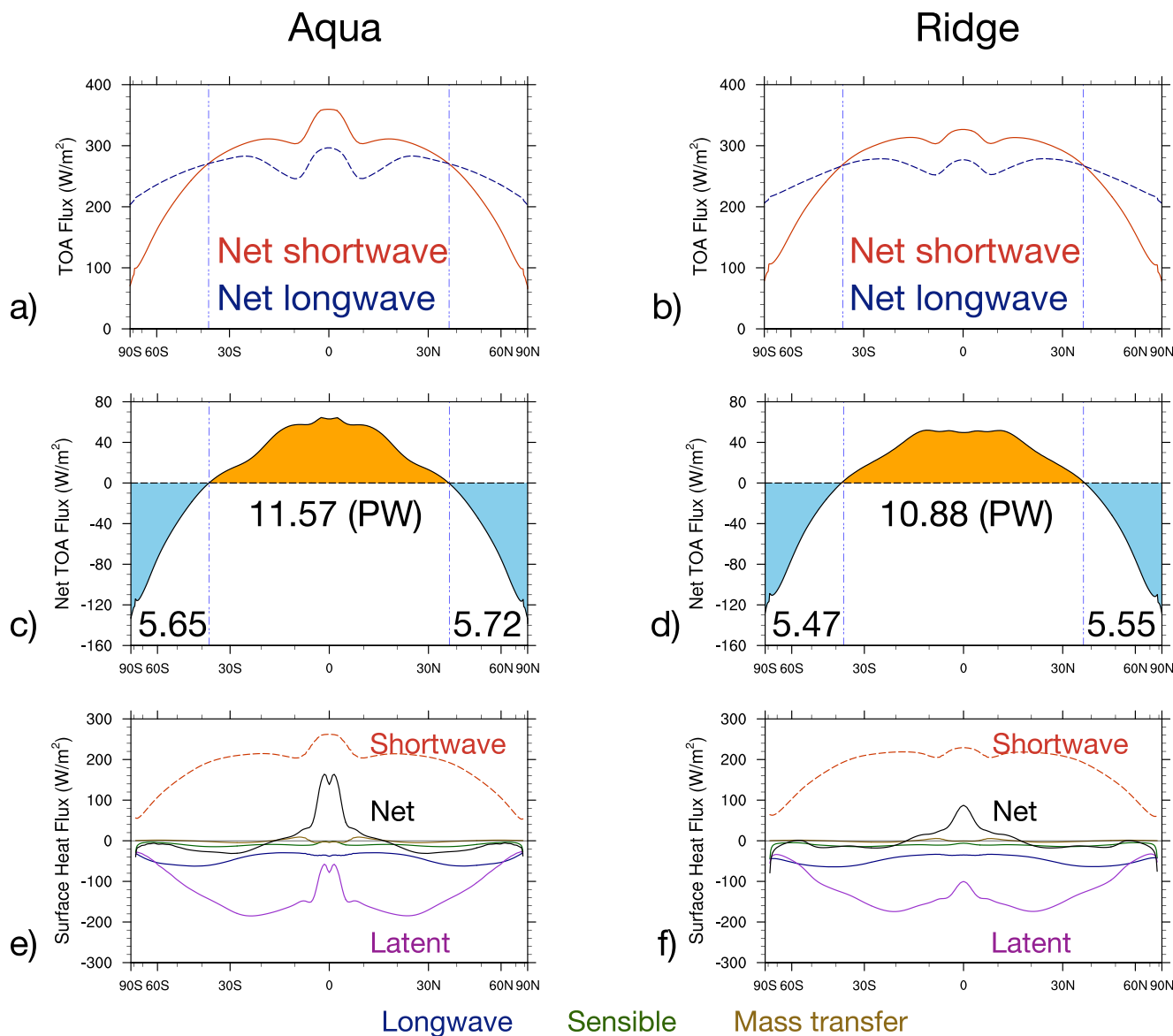


Figure 3. Zonally averaged energy budgets, 100-years climatology. (a–b) Top-of-atmosphere (TOA) fluxes (W m^{-2}). (c–d) Net TOA flux (W m^{-2}) derived from (a–b), labeled with the integrated total amount of tropical surplus (shaded in orange) and extratropical deficit (shaded in blue), in petawatt (PW). (e–f) Ocean surface heat fluxes (W m^{-2}). The x-axis is scaled by $\sin(\text{lat})$ to reflect the proportion of surface area, with minor tick marks at 10° intervals.

cold tongue is a region of greater ocean heating than the rest of tropical Pacific. In this sense, these heating effects are expanded to the entire equatorial cold belt on Aqua, contributing to its warmer climate.

The warmer climate of Aqua corresponds to a more intense water cycle than Ridge. In the global average (Table 1), Aqua's intensified water cycle relative to Ridge is reflected in its slightly higher surface pressure due to water vapor pressure, higher total precipitable water by 18%, and higher precipitation rate by 4.8% (Table 1). The percentage of precipitation increase on Aqua relative to Ridge is consistent with the latent heating of their atmospheres, at a lesser fractional increase than for total precipitable water, as discussed by Pendergrass and Hartmann (2014). Aqua's fractional increase of precipitation with regard to global mean surface temperature is also in line with those reported from CMIP5 warming experiments (Collins et al., 2013). On Aqua, the higher amount of water vapor—a greenhouse gas—helps to maintain its warm state, as shown in the dramatic warming by downwelling longwave compared to Ridge (Table 1). Furthermore, the meridional structures of some relevant fields are shown in Figure 4, and the zonally averaged

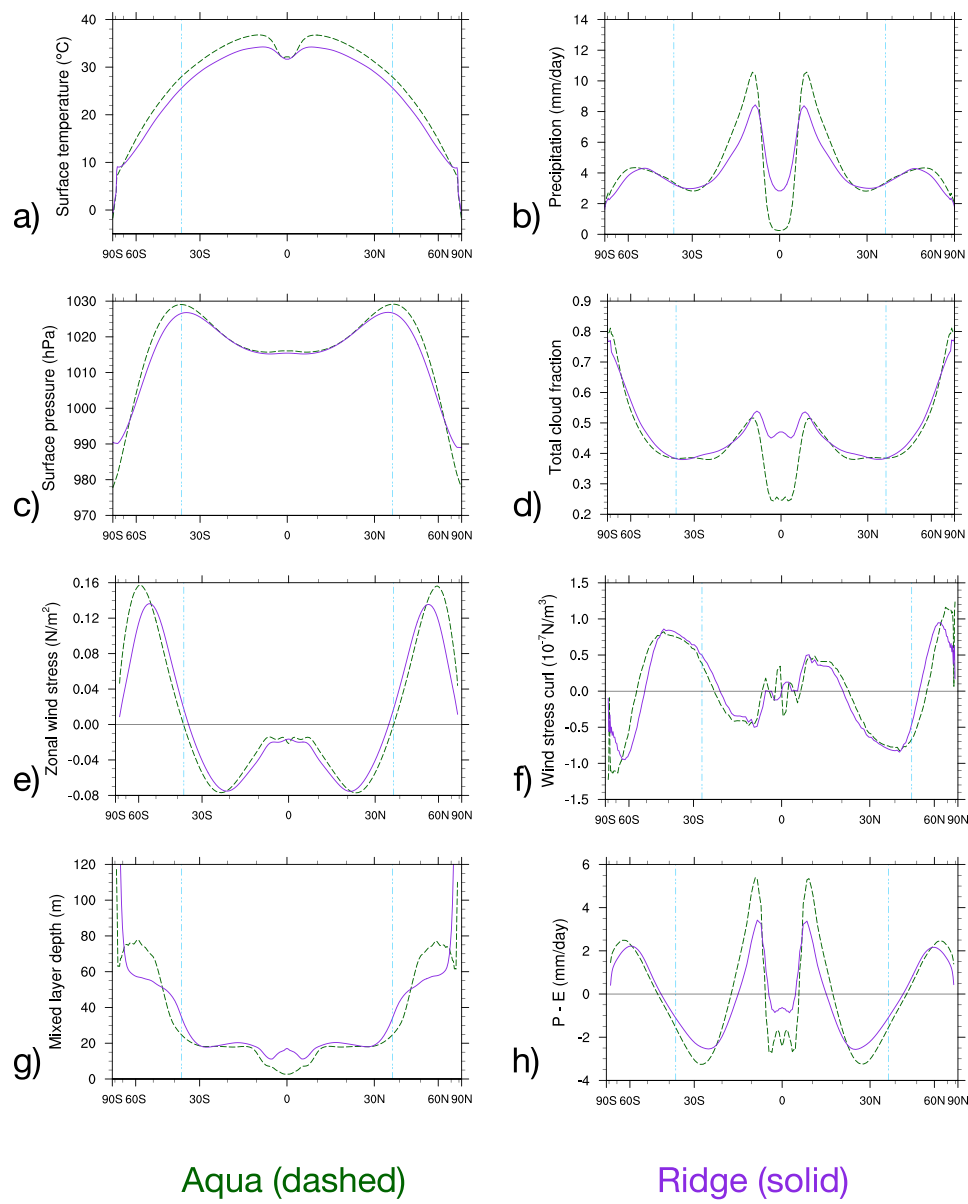


Figure 4. Zonal average profiles, 100-years climatology. (a) Surface temperature ($^{\circ}\text{C}$). (b) Precipitation rate (mm day^{-1}). (c) Surface pressure (hPa). (d) Total cloud fraction (fraction). (e) Zonal wind stress (N m^{-2}). (f) Curl of zonal wind stress (10^{-7} N m^{-3}). (g) Ocean mixed layer depth (m). (h) Precipitation minus evaporation (mm day^{-1}). The vertical blue lines mark the extent of the tropics, as defined by TOA radiative budget (see Figure 3).

vertical structures of moisture and salinity are shown in Figure 5. In the zonal average, both planets have two Intertropical Convergence Zones (ITCZs), with Aqua having higher peaks in precipitation (Figure 4b) and moisture (Figures 5a and 5b) than Ridge. The resulting patterns of freshwater forcing (Figure 4h) correspond to near-surface salinity of the ocean (Figures 5c and 5d). It is worth noting that “double ITCZs” are a common feature of atmosphere-only aquaplanets with prescribed equatorial thermal maximum (Blackburn et al., 2013; Medeiros et al., 2016), and the coupled SST patterns of Aqua and Ridge (Figure 4a) are perhaps even more conducive to such structures.

As defined by the TOA radiative budget in Figure 3, the boundary of the tropics and the descending branch of the Hadley cell (see Figures 8a and 8b and later discussion) coincides with many dynamical features in the zonal average (Figure 4): the peaks in surface pressure (Figure 4c), the switching of direction of zonal wind stress (Figure 4e) and peaks in wind stress curl (Figure 4f), and the deepening of the mixed layer depth

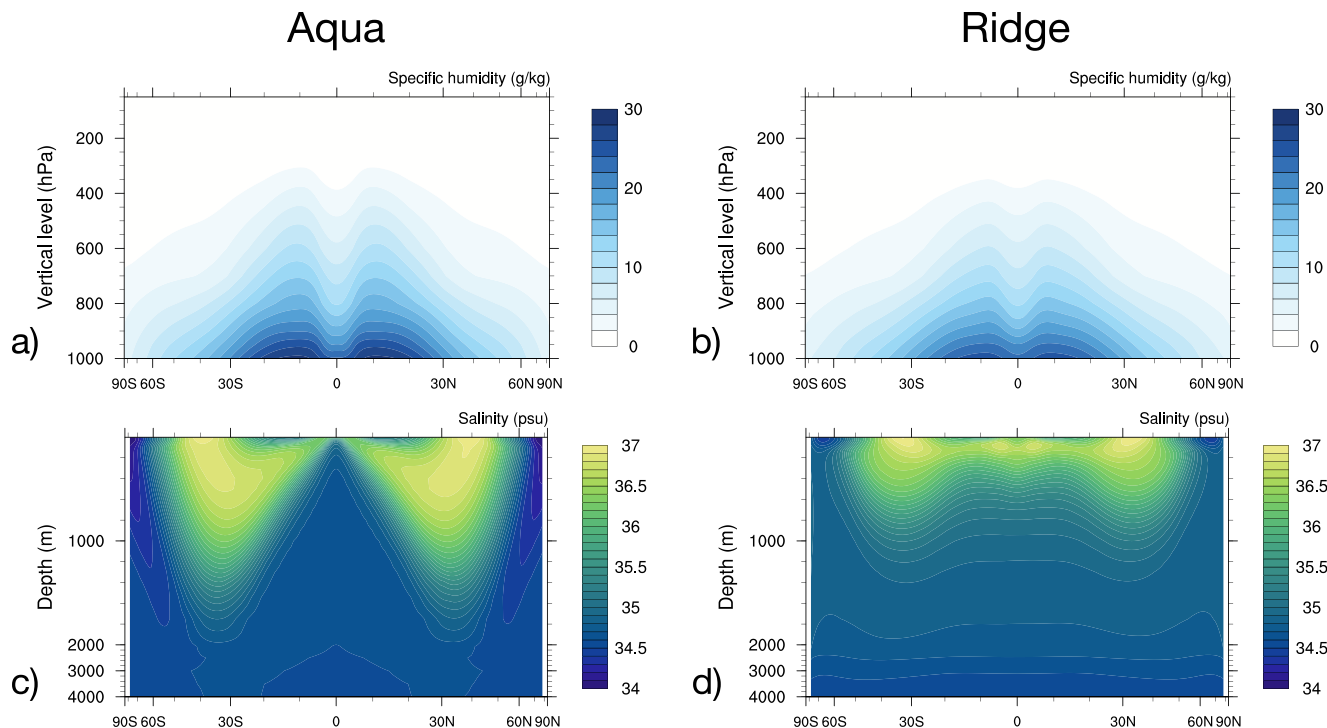


Figure 5. Zonally averaged vertical sections, 100-years climatology. (a–b) Specific humidity (g kg^{-1}). (c–d) Salinity (psu). For the ocean (c–d), the depths below 2,000 m are linearly shrunk as labeled.

toward higher latitudes (Figure 4g). In Figure 4g, the zonal asymmetry in Ridge's tropical thermocline (Figure 2) is responsible for deeper mixed layer depth in the deep tropics than Aqua. These contrasts in the circulation pattern are further discussed in the next subsection.

3.2. Large-Scale Circulation

For both the atmosphere and the ocean, Figure 6 shows features of the horizontal circulation, while Figure 7 shows the vertical structures of the zonally averaged zonal flows.

For the atmosphere, the impact of ocean geometry is mediated by SST. In the surface pressure field (Figures 6a and 6b), compared to Aqua's zonally uniform belt of subtropical high, Ridge has more defined centers of subtropical highs over its eastern boundary currents (see Figure 6b). In the vertical structure, the contrast between the zonally averaged zonal wind of Aqua and Ridge (Figures 7a and 7b; cf. Ch. 15 in Vallis, 2017, on the associations between the meridional temperature gradient, surface wind, and upper-level jets) is influenced by their surface temperature gradients (Figure 4a) through the thermal wind relationship (cf. Enderton & Marshall, 2009). Due to enhanced ocean heat transport to the extratropics via western boundary currents (cf. Enderton & Marshall, 2009; Vallis & Farneti, 2009), the meridional gradient of Ridge's surface temperature is flattened relative to Aqua (Figure 4a). Consequently, the greater surface temperature gradient of Aqua results in greater vertical wind shear, stronger westward flows accumulating upward over the equator, and stronger subtropical and polar jets in the upper levels (Figures 7a and 7b).

For the ocean, the defining horizontal circulations—zonal for Aqua and gyral for Ridge—are shown in Figures 6c and 6d (cf. Ch. 14 in Talley, 2011, on gyres in the Pacific and the Antarctic Circumpolar Current in the Southern Ocean). On zonally unbounded Aqua, the rapid zonal flows result in $\sim 1,800 \text{ Sv}$ of globally integrated net zonal transport. On bounded Ridge, the gyral flows $\sim O(100) \text{ Sv}$ arise from Sverdrup dynamics, corresponding to the meridional distribution of surface wind stress (Figures 4e and 4f). These gyres suggest analogs of the Pacific's equatorial counter-currents and the western and eastern boundary systems. Figures 7c and 7d present the zonally averaged vertical structure of these currents in the zonal direction. On Aqua (Figure 7c), the direction of the zonal currents corresponds to the surface wind stress (Figure 4c), with

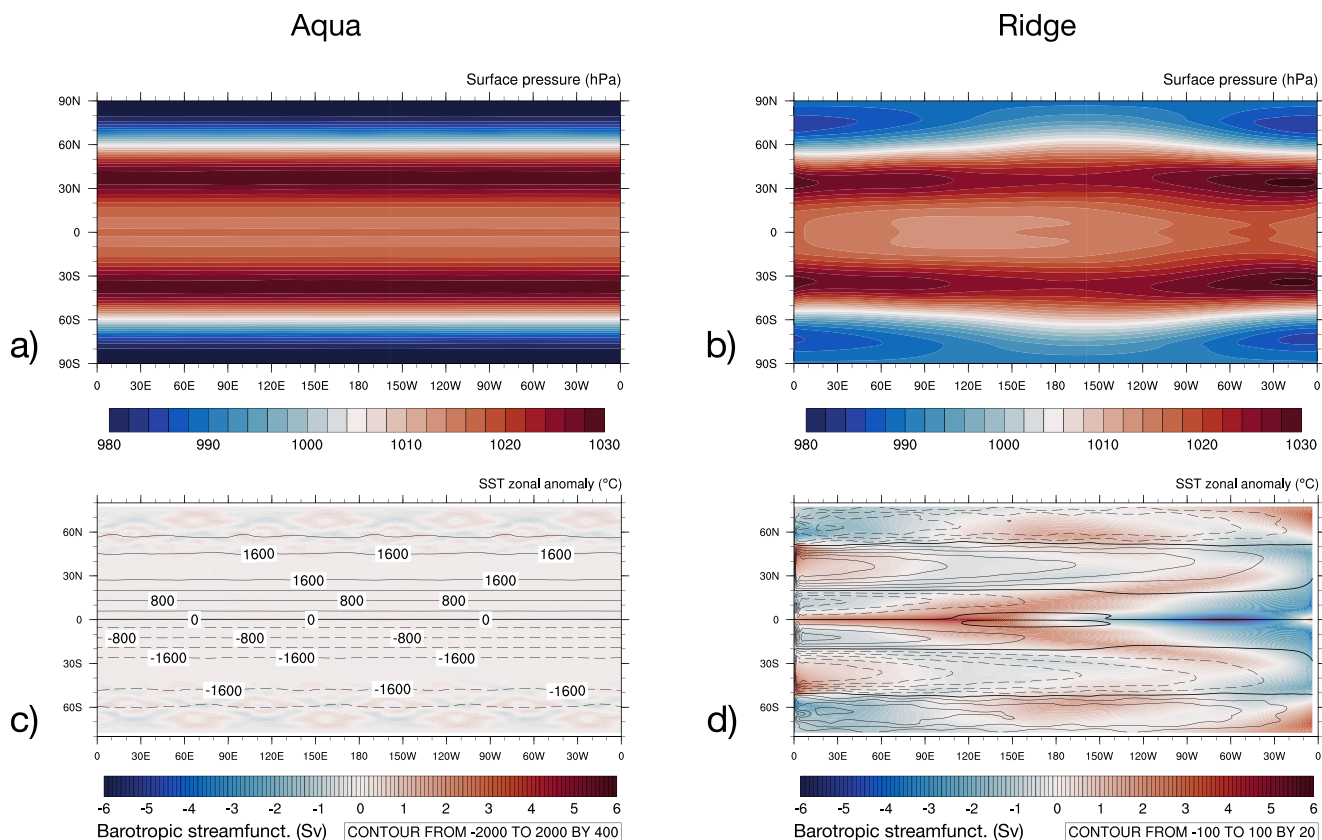


Figure 6. Plan views of 100-years climatology. (a–b) Atmosphere: surface pressure (hPa). (c–d) Ocean: barotropic streamfunction (Sv, contour lines; solid is positive/clockwise, dashed is negative/counter-clockwise), overlaid on the zonal anomaly of SST ($^{\circ}$ C, color shading). Note the difference in contouring intervals for the streamfunction (c–d). The pattern of Aqua's SST zonal anomaly (panel c), barely visible, reflects the imprints of bottom topography.

velocity dampening toward zero deeper down. Near the surface, the maximum velocity of the westward current reaches 2.29 m s^{-1} . Ridge, in contrast, shows richer structure particularly in the tropics, with the presence of equatorial under- and counter-currents (Figure 7d). The depth of the equatorial undercurrent at $\sim 200 \text{ m}$ is consistent with the depth of the equatorial thermocline (Figure 2i). These features are absent on Aqua, which cannot maintain zonal pressure gradients in its interior. Ridge's maximum velocity, in the near-surface equatorial westward current, is 0.44 m s^{-1} , about an order of magnitude lower than Aqua's. The effect of Ridge's meridional boundary is also seen in the meridional overturning circulation of both the atmosphere and the ocean (Figure 8). For the atmosphere, in addition to the more familiar-looking overturning cells, the equatorial cold belt on Aqua leads to the formation of “reverse Hadley” cells in the deep tropics. On Ridge, this pattern is largely suppressed due to the western warm pool (Figure 2, right column) that reduces the meridional gradient around the equatorial SST minimum in the zonal average (Figure 4a). For the ocean, Aqua's residual overturning broadly follows the isopycnals (Marshall & Radko, 2003; Wolfe & Cessi, 2011), forming deep subtropical cells (Figure 8c). Alternatively, the residual overturning can be interpreted as the combination of the Eulerian mean and eddy components (see Figure S4), where the compensating effect between the two components at high latitudes is analogous to the vanishing Deacon cell in the Southern Ocean (cf. Marshall et al., 2007; Smith et al., 2006). For Ridge, the presence of zonal pressure gradient largely reduces the depth of the subtropical overturning cells. Under the influence of polar convection, the mid-depth ($\sim 1,000 \text{ m}$), diapycnal overturning cells in the midlatitudes are maintained by the balance between cooling via upwelling and diffusive heating (W. H. Munk, 1966; W. Munk & Wunsch, 1998).

An intriguing consequence of the “reverse Hadley” cells is observed in the seasonality of the ITCZs. Figure 9 shows the meridional migration of zonally averaged precipitation pattern with the seasonal cycle, in relation to surface temperature. For Ridge, an increase in precipitation—maximum 3.7 mm day^{-1} —is present in the summer hemisphere, corresponding to the seasonal warming of SST (Figure 9b). However, for

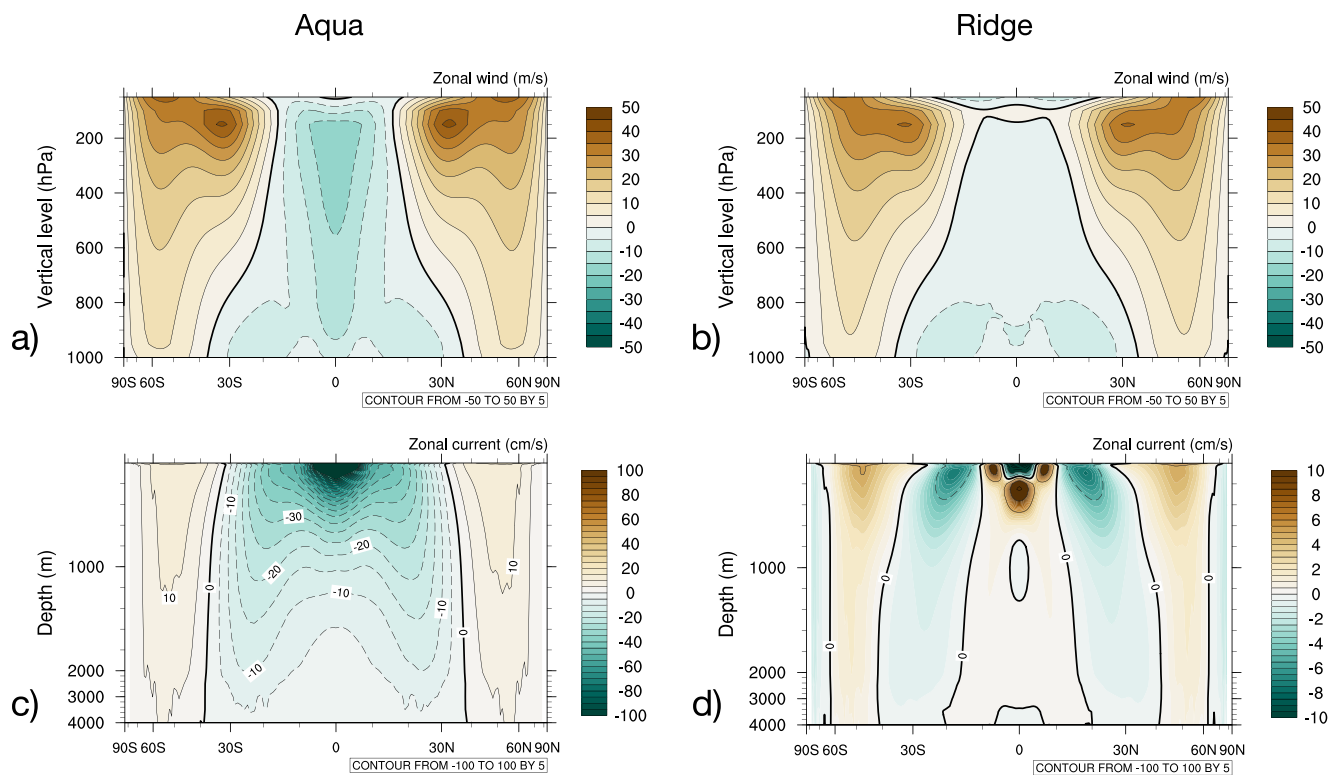


Figure 7. Zonally averaged vertical sections, 100-years climatology. (a–b) Atmosphere: zonal wind (m s^{-1}). (c–d) Ocean: zonal current (cm s^{-1}). The color scale of panel (c) is an order of magnitude greater than panel (d).

Aqua, although the pattern of precipitation increase between $\sim 10^\circ\text{--}20^\circ$ latitude in the summer hemisphere is similar to Ridge, it is the winter hemisphere that shows even greater increase in precipitation, reaching 5.7 mm day^{-1} at maximum (Figure 9a). The circulation pattern underlying this counter-intuitive behavior is further examined focusing on boreal summer (June, July, and August; JJA); boreal winter is a mirror image due to the hemispheric symmetry of these two models. Figure 10 shows the zonally averaged profiles of surface temperature and precipitation in JJA, and Figure 11 shows the corresponding atmospheric meridional overturning circulation in JJA. For Aqua, despite higher SST in the summer hemisphere (Figure 10a), its peak precipitation is in the winter hemisphere (Figure 10b) as seen in Figure 9a. This is a consequence of the persistence of Aqua's equatorial cold belt throughout the seasonal cycle, which creates a stand-alone “reverse Hadley” cell in the winter hemisphere (Figure 11a) over the local SST minimum (Figure 10a). The ascending branch of this overturning cell, at $\sim 10^\circ$ latitude in the winter hemisphere, creates a narrow but extreme band of maximum precipitation (Figure 10b) exceeding that of the summer hemisphere. In this regard, Ridge behaves more Earth-like (cf. Ch 11 in Holton & Hakim, 2012, on the association between Earth's ITCZ and Hadley circulation): in the winter or summer season, although the presence of the eastern cold tongue manifests itself by affecting the magnitude of the cross-equatorial Hadley-like overturning (Figure 11b), dynamically its convection-inducing effects in the winter flank are much reduced compared to Aqua's case. For this reason, the zonally averaged maximum precipitation of Ridge remains in the summer hemisphere (Figure 10b). As suggested by the similarly counter-intuitive seasonal distribution of Aqua's atmospheric moisture in Figure 1c, this is yet another subtle aspect of how ocean geometry governs the state of the coupled climate, including the interaction between the large-scale circulation and the water cycle. More broadly, the seasonality of the meridional overturning cells in Figure 11—and the associated meridional heat transport—is tied to the viewpoint of “energy flux equator” that modulates ITCZ migration on various time scales (e.g., Kang et al., 2008; Schneider et al., 2014). Although a comprehensive analysis on this topic is beyond the scope of the present study, future investigations taking advantage of the fully represented ocean dynamics will likely be revealing.

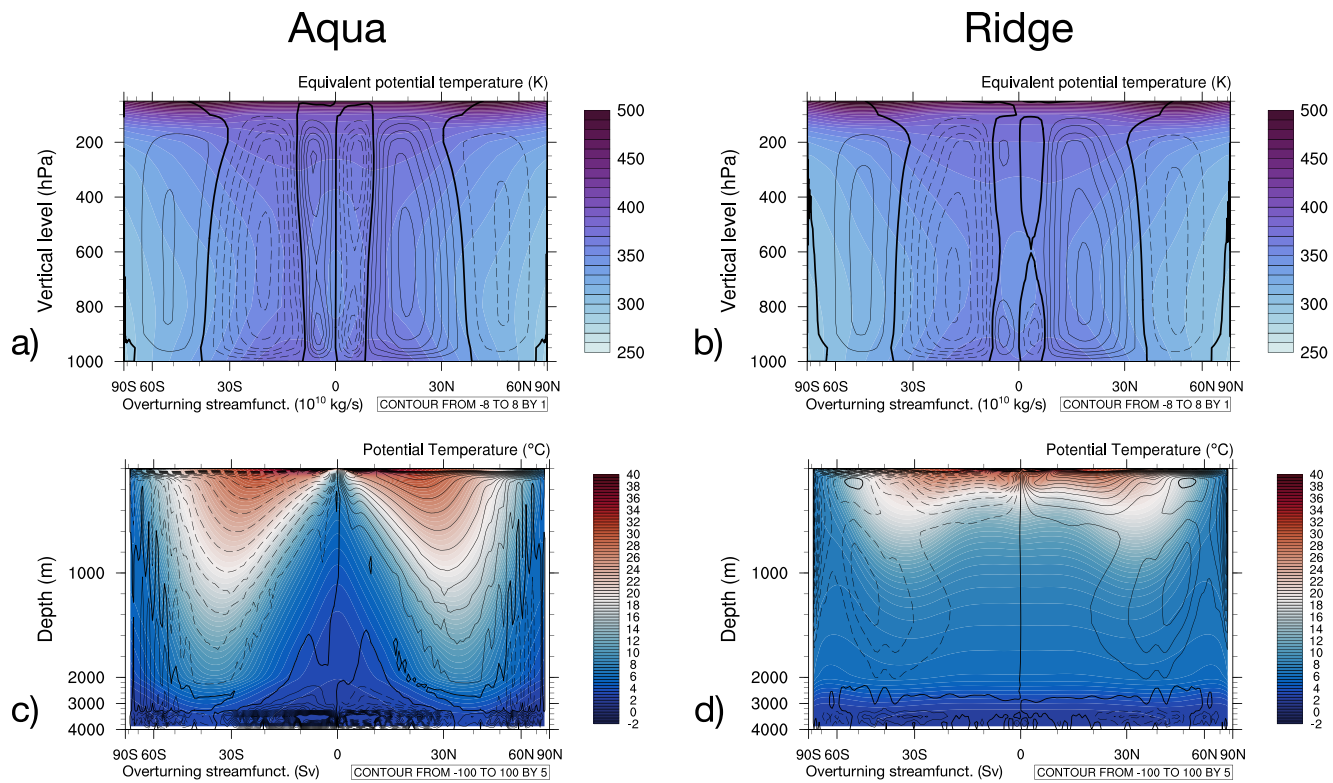


Figure 8. Zonally averaged vertical sections, 100-years climatology. (a–b) Atmosphere: Eulerian meridional overturning streamfunction ($10^{10} \text{ kg s}^{-1}$, contour lines; solid is positive/clockwise, dashed is negative/counterclockwise), overlaid on equivalent potential temperature (K, colored shading). (c–d) Ocean: residual overturning streamfunction (Sv, contour lines; solid is positive/clockwise, dashed is negative/counterclockwise), overlaid on potential temperature ($^{\circ}\text{C}$, colored shading). The overturning cells in the ocean are closed to within the magnitude of atmospheric moisture transport in the surface mixed layer (see P–E in Figure 4h).

3.3. Meridional Heat Transport

The energy budget and circulation patterns of the two planets, as described by the previous subsections, drive the meridional heat transport (Figure 12). For both planets, the total meridional heat transport peaks close to 6 PW in each hemisphere, at the bounds of the tropics. Ocean heat transport, dominating in the deep tropics, peaks at close to 4 PW for Aqua, and around 2 PW for Ridge. Atmospheric heat transport, dominating in the extratropics, peaks around 50°N/S for both planets. Overall, as discussed by Enderton and Marshall (2009), the qualitative features and partition between the atmosphere and the ocean resemble Earth observations (Fasullo & Trenberth, 2008), with Ridge showing greater degrees of realism. Here we discuss the differences between Aqua and Ridge from energetic and dynamic perspectives (Armour et al., 2019).

Energetically, the TOA tropical surplus (Figures 3c and 3d) requires greater amounts of total meridional heat transport for Aqua than Ridge. Likewise, the excessive net heating of Aqua's tropical ocean (Figure 3e) results in greater amounts of ocean heat transport out of the tropics than Ridge (Figure 3f). In particular, over the equatorial region, since the net heating at ocean surface exceeds that of TOA, it is implied that the atmosphere must compensate by transporting energy equatorward for those regions (Figure 12).

Dynamically, these requirements are fulfilled by the meridional overturning circulation in both fluids (Figure 8). As detailed in Czaja and Marshall (2006), the meridional heat transport by either fluid can be viewed as decomposed into two factors: the magnitude of the meridional overturning, and the energy contrast between the poleward and equatorward branches, as measured by moist static energy for the atmosphere and potential temperature for the ocean. For the atmosphere, the equatorward heat transport over 10°N/S is delivered by the “reverse Hadley” cells (Figures 8a and 8b), which transport higher amounts of moist static energy in their equatorward upper branches than their poleward lower branches, at greater magnitude of

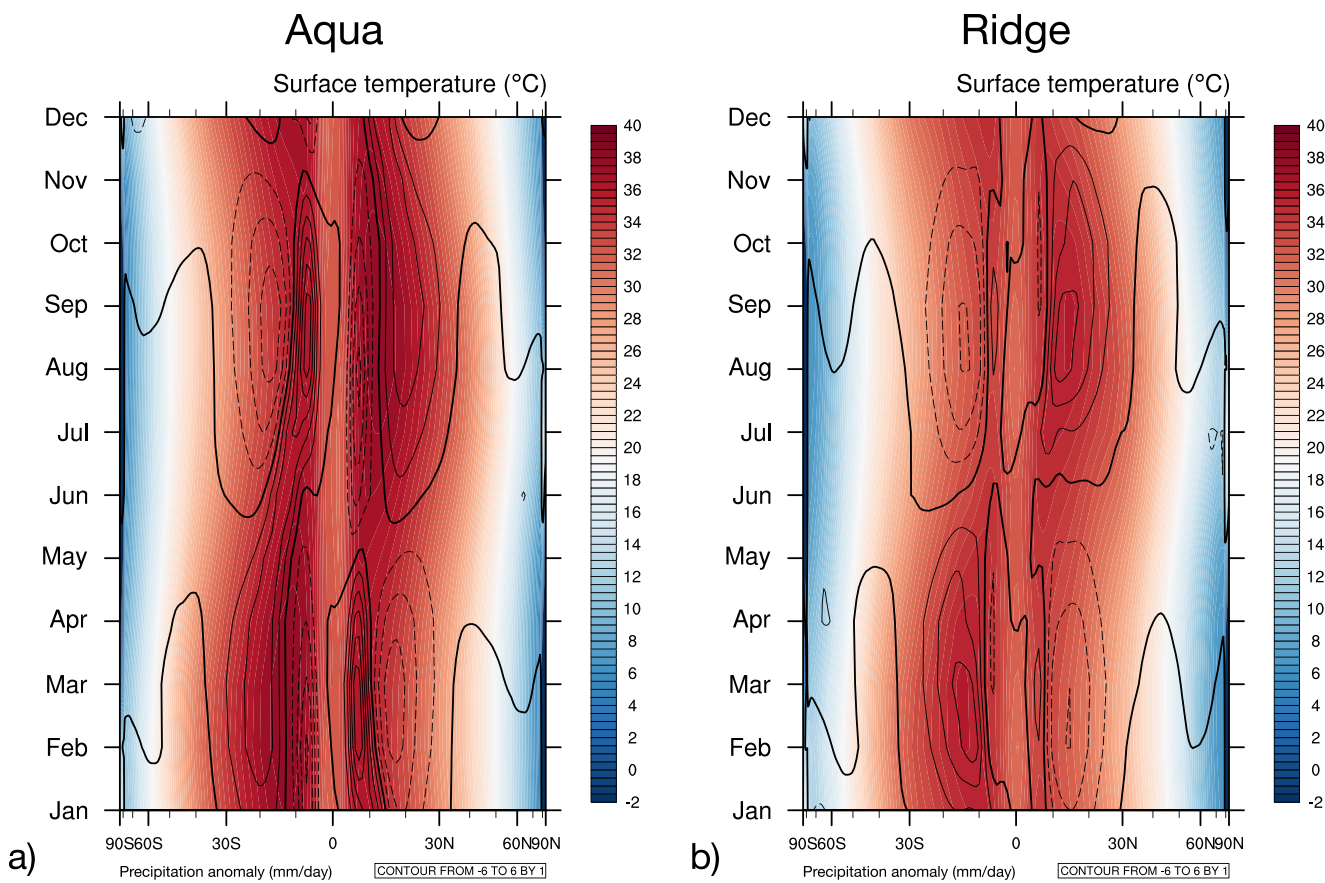


Figure 9. The seasonal cycle of zonally averaged surface temperature ($^{\circ}\text{C}$, colored shading) and precipitation anomaly from the annual mean (mm day^{-1} , contour lines; solid is positive, dashed is negative), 100-years climatology. (a) Aqua. (b) Ridge.

overturbing on Aqua than Ridge. It is worth noting that the Eulerian mean overturning in Figures 8a and 8b only reflects the atmospheric heat transport by the mean flow, which dominates in the tropics, but gives way to the eddy component at higher latitudes (cf. Enderton & Marshall, 2009). For the ocean, the energetically required ocean heat transport is accomplished by the residual overturning (Figures 8c and 8d), where the thermal contrast between the poleward upper branch and equatorward lower branch is greater on Aqua

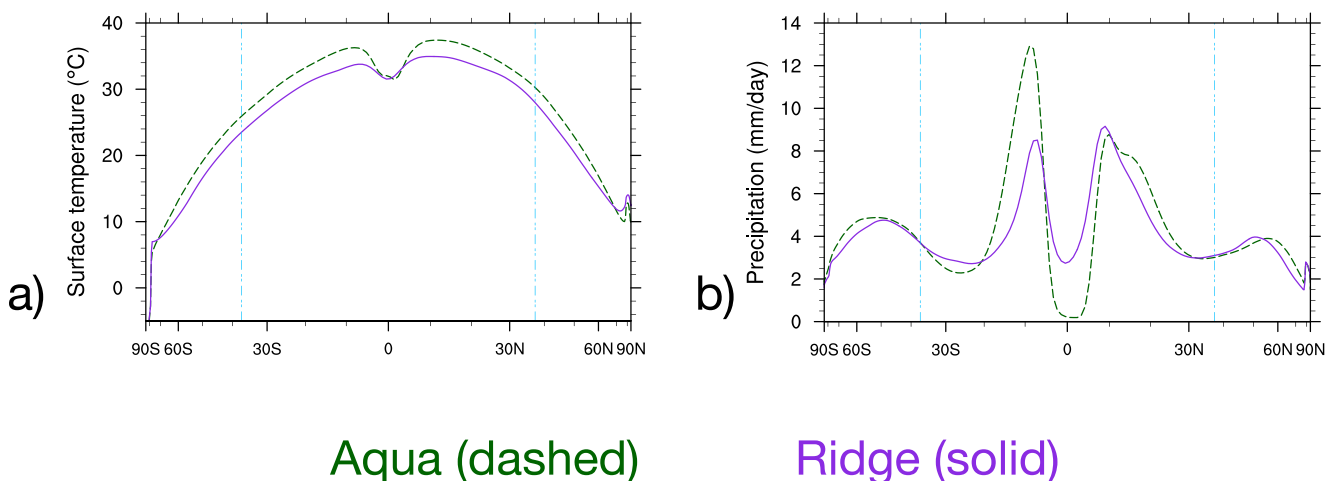


Figure 10. As Figures 4a and 4b, but for boreal summer (June, July, and August).

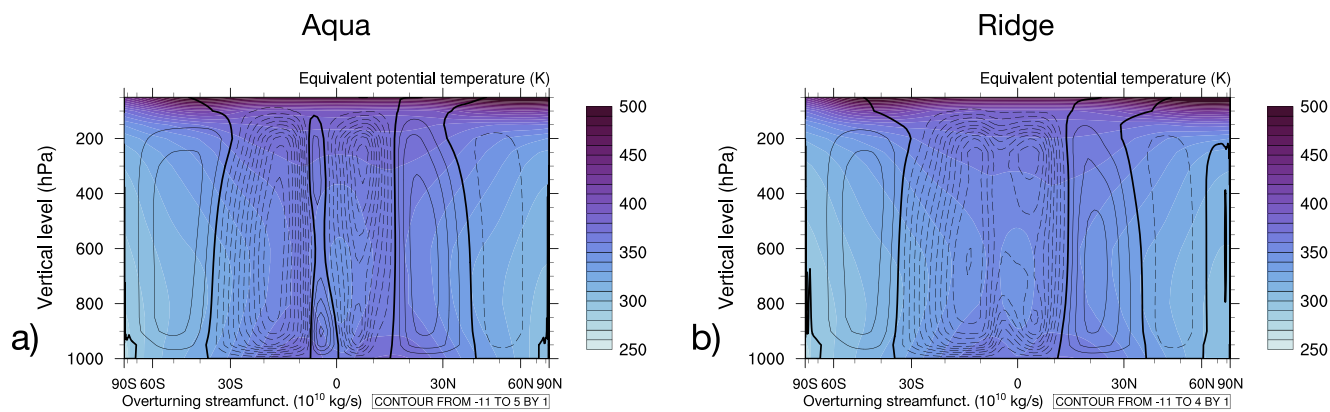


Figure 11. As Figures 8a and 8b, but for boreal summer (June, July, and August).

than Ridge, as the equatorward branch of Aqua's residual overturning reaches near the bottom. On Ridge (Figure 12b), the “kinks” in ocean heat transport, or local maximum at $\sim 20^{\circ}\text{N/S}$ and local minimum at $\sim 50^{\circ}\text{N/S}$, reflect the boundary of the gyres (Figure 6d), absent on Aqua.

Overall, this comparison highlights the influence of the meridional boundary on meridional heat transport and its partition, via both the energetic requirements and the dynamics (Czaja & Marshall, 2006; Enderton & Marshall, 2009). Particularly, in light of having better resolved “reverse Hadley” circulation than earlier investigations (Czaja & Marshall, 2006; Farneti & Vallis, 2009; Smith et al., 2006) and the corresponding equatorward heat transport by the atmosphere, we note the role of Ridge's meridional boundary in shaping a more Earth-like pattern of meridional heat transport.

4. Conclusions and Discussion

In this study, we introduce the first two examples of fully coupled, idealized models developed in the CESM Simpler Models framework. Building upon previous idealized studies using aquaplanets at various degrees of complexity and atmosphere-ocean coupling, our work explores the coupled climate controlled by ocean geometry, represented by a meridional boundary present on Ridge and absent on Aqua. By using contemporary atmospheric and ocean model components at resolutions comparable to comprehensive Earth System Models, we aim to apply these idealized models to gain insight into the more complex features of realistic coupled climate models.

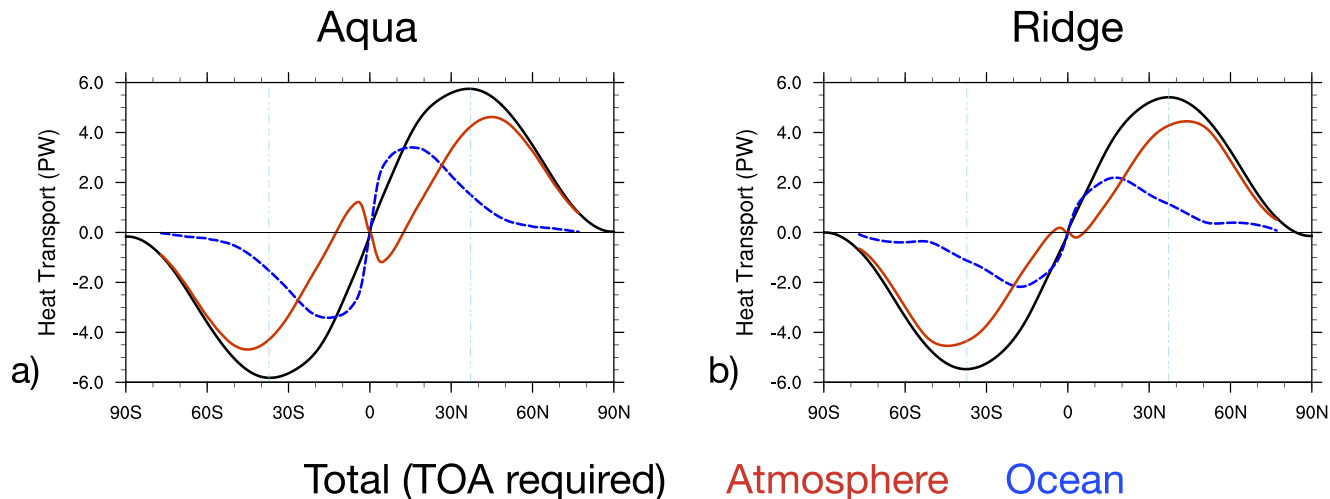


Figure 12. Meridional heat transport, 100-years climatology. (a) Aqua. (b) Ridge. The vertical blue lines mark the extent of the tropics, as in Figures 3a–3d and Figure 4.

Contrasting the mean climates of the CESM Aqua and Ridge planets, the main conclusions are summarized as follows:

1. With sufficient horizontal and vertical resolution, Aqua manifests a global cold belt of equatorial upwelling, while Ridge develops zonal contrast between its western warm pool and eastern cold tongue due to boundary dynamics.
2. Energetically, Aqua's cold belt results in a climate state $\sim 2^{\circ}\text{C}$ warmer than Ridge on global average, due to the effects of tropical clouds and water vapor.
3. Dynamically, the meridional boundary of Ridge—with the resulting zonal asymmetry—is crucial for producing a climate system with more Earth-like features compared to Aqua, including atmospheric and ocean circulation, the seasonality of ITCZ, and the meridional heat transport.

In general, the CESM Aqua and Ridge planets present a number of qualitative features similar to those discussed by previous works (Enderton & Marshall, 2009; Farneti & Vallis, 2009; Smith et al., 2006), including the large-scale circulation and meridional heat transport. We discuss the following characteristics of the two coupled models that differ significantly from previous studies:

1. *The climate contrast between Aqua and Ridge and the role of ocean geometry in planetary albedo.* Contrary to Enderton and Marshall (2009) where Aqua—with its sea ice—has a colder climate than the ice-free Ridge, in the present study ice-free CESM Aqua is warmer than Ridge. As discussed in Section 3.1, this is attributed to the tropical distribution of clouds, which largely dominates the planetary albedo in the absence of ice. Compared to ice-present climate states of Enderton and Marshall (2009), the contrast between ice-free Aqua and Ridge suggests a fundamentally different role of the ocean's meridional boundary on the global climate: instead of reducing planetary albedo by the melting of sea ice via the ocean's western boundary dynamics, the strip continent in CESM Ridge enhances planetary albedo through tropical clouds, via the formation of the western warm pool and atmospheric convection over it. While the quantitative effect likely depends on configurations of the atmospheric model including resolution, parameterization, and other aspects affecting the representation of clouds (cf. apparently minimized contrast between the Aqua and Ridge configurations in Smith et al., 2006), the qualitative contrast with Aqua has implications for the investigation of ice-free warm states in Earth's history or future.
2. *Aqua's equatorial cold belt and the resulting "reverse Hadley" circulation, with relevance to realistic models.* In CESM Aqua, the atmospheric "reverse Hadley" cells over the equatorial belt of upwelling are more distinctively represented than earlier models (Farneti & Vallis, 2009; Marshall et al., 2007; Smith et al., 2006), providing stronger contrast against the corresponding Ridge configuration. While the coupled tropical dynamics of wind-driven equatorial upwelling and the corresponding atmospheric "reverse Hadley" cells are relatively straightforward, the representation of these features likely depends on the horizontal resolution of both model components for resolving the oceanic belt of upwelling and the narrow (less than 10° in the meridional extent) atmospheric cells. Since wind-driven upwelling is a fundamental mechanism of the eastern Pacific cold tongue, CESM Aqua provides a unique reduced-complexity configuration with boundary dynamics removed. By using model components and resolution comparable to that of CMIP, the assessment of these features—comparative to Ridge or additional forms of ocean geometry—will have implications for the representation of the eastern Pacific cold tongue, the corresponding regional meridional cells (e.g., Sun et al., 2019), and associated climate variability (e.g., Chen et al., 2017) in realistic, coupled Earth configurations.
3. *The location and intensity of Ridge's western warm pool, as an analog to the Pacific.* Compared to earlier Ridge models with a warm pool closer to the western boundary and a relatively weak zonal SST gradient (Enderton & Marshall, 2009; Farneti & Vallis, 2009; Smith et al., 2006), CESM Ridge has a climatological warm pool farther east (distance from the western boundary $\sim 1/3$ of the basin width), and a zonal SST gradient comparable to the Pacific. Interestingly, the relative location of CESM Ridge's warm pool is surprisingly Pacific-like, despite the total lack of the Maritime Continent or other topographic details. This invites the question of differentiating between coincidental resemblance and potential control by fundamental, robust mechanisms. Besides ocean dynamics, previous studies on the western Pacific have pointed to the roles of cloud forcing and wind stress in shaping the warm pool (e.g., Burls & Fedorov, 2014; Clement et al., 2005; Watanabe, 2008a, 2008b). Further investigations of these mechanisms can be facilitated by this coupled, idealized framework.

In terms of broader applications, as presented in Section 3 and discussed above, the current configuration of the CESM Aqua and Ridge planets can be used for the investigation of a range of topics particularly relatable to the tropical Pacific. Furthermore, preliminary analysis on the sub-seasonal to interannual variability of Aqua and Ridge reveals promising features, including MJO- and ENSO-like modes on Ridge. These modes of tropical variability, in different forms for Aqua and Ridge with relevance to the interpretation of realistic Earth configurations, will be addressed in future work. As the design of idealized models depends on the question to be addressed, we also discuss here a few directions in which to expand the coupled simplified configurations, for the investigation of topics that are beyond the scope of the present study. Building on the two baseline configurations of Aqua and Ridge, these expansions can potentially be configured with relative ease:

1. Increased atmospheric and/or ocean resolution comparable to that of the High Resolution Model Intercomparison Project (HighResMIP; Haarsma et al., 2016) for a broader range of scale interactions and process-level studies. Examples include tropical cyclones for the atmospheric component, and improved representation of boundary currents for the ocean component. While the computational cost associated with higher resolution can be an obstacle, the present Aqua and Ridge climate states can facilitate the process as reasonably equilibrated starting points.
2. Alternative parameter choices for ice-ocean-atmosphere interactions. In the same spirit as Medeiros et al. (2016), there is no unique or correct idealized CESM configuration. When desired, colder climate states with sea ice at high latitudes can potentially be achieved by design. The tuning of convective parameters in the atmospheric component is a well-known factor that affects the global energy budget, mostly through clouds (e.g., Yang et al., 2013). Land properties of the polar caps in the present models—particularly surface albedo—may likewise affect the energy balance through the surface albedo feedback (e.g., Hall, 2004). Changes in the forcing such as solar insolation, greenhouse gases, or aerosol may also lead to significant responses. The sensitivity of the coupled idealized models to such choices can be a topic of future studies.
3. Additional ocean geometries (e.g., Ferreira et al., 2010). The representation of ocean features such as the interhemispheric Atlantic meridional overturning circulation may require opening up the Drake passage (e.g., Enderton & Marshall, 2009; Johnson et al., 2019, and references therein). The investigation of inter-basin interactions would require an additional continent(s) to separate the ocean basins, with relevance to generalized understanding or specific paleoclimate questions (e.g., Ferreira, Marshall, & Campin, 2010; Ferreira, Marshall, Ito et al., 2018; Tabor et al., 2019). An optimistic expectation is that with community development, a hierarchy of increasingly complex and realistic ocean geometries in the idealized coupled modeling framework will be informative for understanding the behavior of more comprehensive Earth configurations.

To conclude, the climate states of CESM Aqua and Ridge configurations showcase the capability of the idealized coupled models to represent relatively well-understood dynamics, while further enabling more detailed investigation of the coupled climate system. The newly available capability—including aspects of cloud radiative effects, convection, and circulation—are due to increased resolution and more complete physics of CMIP-class components. By using CESM components, the close relationship between these idealized configurations and comprehensive, realistic Earth configurations fills a long-standing gap in the idealized modeling hierarchy. This addition to the hierarchy opens up new potential for the investigation of coupled atmosphere-ocean processes, as well as serving as test beds for model evaluation and development. The Aqua and Ridge configurations presented here are expected to be available in the next major release of CESM as part of the Simpler Models suite, potentially with the software for creating additional, customized ocean geometries.

Data Availability Statement

The model case directories and the simulation outputs under analysis are available at <https://doi.org/10.5281/zenodo.4646251>, and on CISL's Globally Accessible Data Environment. The CESM source code is available at www.cesm.ucar.edu.

Acknowledgments

We thank the following collaborators for their help with simplified climate models (in alphabetical order): Alper Altuntas, Kyle Armour, David Bailey, Jim Benedict, Pedro DiNezio, Erik Kluzeck, Keith Lindsay, Brian Medeiros, Sarah Ragen, Mathew Rothstein, and Andrew Shao. We also thank Anna-Lena Deppenmeier for helpful discussion on the writing, and two reviewers for their constructive comments that helped to improve the quality and presentation of this manuscript. Wu was supported by National Science Foundation (NSF) grant AGS1648629, the Advanced Study Program of NCAR, and the Junior Researcher Award of the Institute for Advanced Computational Science at Stony Brook University. Reed was supported by NSF grants AGS1648629 and AGS1830729. The National Center for Atmospheric Research (NCAR) is sponsored by the NSF under Cooperative Agreement 1852977. We acknowledge computing and data storage resources, including the Cheyenne supercomputer (<http://doi.org/10.5065/D6RX99HX>), provided by the Computational and Information Systems Laboratory (CISL) at NCAR.

References

- Abernathey, R., Ferreira, D., & Klocker, A. (2013). Diagnostics of isopycnal mixing in a circumpolar channel. *Ocean Modelling*, 72, 1–16. <https://doi.org/10.1016/j.ocemod.2013.07.004>
- Adcroft, A., Anderson, W., Balaji, V., Blanton, C., Bushuk, M., Dufour, C. O., et al. (2019). The GFDL global ocean and sea ice model OM4.0: Model description and simulation features. *Journal of Advances Model Earth Systems*, 11(10), 3167–3211. <https://doi.org/10.1029/2019ms001726>
- Armour, K. C., Siler, N., Donohoe, A., & Roe, G. H. (2019). Meridional atmospheric heat transport constrained by energetics and mediated by large-scale diffusion. *Journal of Climate*, 32(12), 3655–3680. <https://doi.org/10.1175/jcli-d-18-0563.1>
- Bachman, S., & Fox-Kemper, B. (2013). Eddy parameterization challenge suite I: Eady spindown. *Ocean Modelling*, 64, 12–28. <https://doi.org/10.1016/j.ocemod.2012.12.003>
- Bailey, D., DuVivier, A., Holland, M., Hunke, E., Lipscomb, B., Briegleb, B., et al. (2018). CESM CICE5 users guide (Tech. Rep.). Tech. rep.
- Ballinger, A. P., Merlis, T. M., Held, I. M., & Zhao, M. (2015). The sensitivity of tropical cyclone activity to off-equatorial thermal forcing in aquaplanet simulations. *Journal of the Atmospheric Sciences*, 72(6), 2286–2302. <https://doi.org/10.1175/jas-d-14-0284.1>
- Benedict, J. J., Medeiros, B., Clement, A. C., & Pendergrass, A. G. (2017). Sensitivities of the hydrologic cycle to model physics, grid resolution, and ocean type in the aquaplanet Community Atmosphere Model. *Journal of Advances in Modeling Earth Systems*, 9(2), 1307–1324. <https://doi.org/10.1002/2016ms000891>
- Blackburn, M., Williamson, D. L., Nakajima, K., Ohfuchi, W., Takahashi, Y. O., Hayashi, Y.-Y., et al. (2013). The aqua-planet experiment (APE): Control SST simulation. *Journal of the Meteorological Society of Japan*, 91A, 17–56. <https://doi.org/10.2151/jmsj.2013-a02>
- Bleck, R. (1978). On the use of hybrid vertical coordinates in numerical weather prediction models. *Monthly Weather Review*, 106(9), 1233–1244. [https://doi.org/10.1175/1520-0493\(1978\)106<1233:otuohv>2.0.co;2](https://doi.org/10.1175/1520-0493(1978)106<1233:otuohv>2.0.co;2)
- Brunetti, M., Kasparian, J., & Vérard, C. (2019). Co-existing climate attractors in a coupled aquaplanet. *Climate Dynamics*, 53(9–10), 6293–6308. <https://doi.org/10.1007/s00382-019-04926-7>
- Burls, N. J., & Fedorov, A. V. (2014). What controls the mean east-west sea surface temperature gradient in the equatorial Pacific: The role of Cloud Albedo. *Journal of Climate*, 27(7), 2757–2778. <https://doi.org/10.1175/jcli-d-13-00255.1>
- Carranza, M. M., Gille, S. T., Franks, P. J. S., Johnson, K. S., Pinkel, R., & Girton, J. B. (2018). When mixed layers are not mixed. Storm-driven mixing and bio-optical vertical gradients in mixed layers of the Southern Ocean. *Journal of Geophysical Research: Oceans*, 123(10), 7264–7289. <https://doi.org/10.1029/2018jc014416>
- Cessi, P., & Jones, C. S. (2017). Warm-route versus cold-route interbasin exchange in the meridional overturning circulation. *Journal of Physical Oceanography*, 47(8), 1981–1997. <https://doi.org/10.1175/jpo-d-16-0249.1>
- Chang, K.-I., Ghil, M., Ide, K., & Lai, C.-C. A. (2001). Transition to aperiodic variability in a wind-driven double-gyre circulation model. *Journal of Physical Oceanography*, 31(5), 1260–1286. [https://doi.org/10.1175/1520-0485\(2001\)031<1260:ttavia>2.0.co;2](https://doi.org/10.1175/1520-0485(2001)031<1260:ttavia>2.0.co;2)
- Chavas, D. R., Reed, K. A., & Knaff, J. A. (2017). Physical understanding of the tropical cyclone wind-pressure relationship [Journal Article]. *Nature Communications*, 8(1), 1360. <https://doi.org/10.1038/s41467-017-01546-9>
- Chen, C., Cane, M. A., Wittenberg, A. T., & Chen, D. (2017). ENSO in the CMIP5 simulations: Life cycles, diversity, and responses to climate change. *Journal of Climate*, 30(2), 775–801. <https://doi.org/10.1175/jcli-d-15-0901.1>
- Clement, A. C., Seager, R., & Murtugudde, R. (2005). Why are there tropical warm pools? *Journal of Climate*, 18(24), 5294–5311. <https://doi.org/10.1175/jcli3582.1>
- Collins, M., Knutti, R., Arblaster, J., Dufresne, J.-L., Fichefet, T., & Friedlingstein, P., et al. (2013). Long-term climate change: Projections, commitments and irreversibility. *Climate change 2013—the physical science basis: Contribution of working group I to the fifth assessment report of the intergovernmental panel on climate change* (pp. 1029–1136). Cambridge University Press.
- Czaja, A., & Marshall, J. (2006). The partitioning of poleward heat transport between the atmosphere and ocean. *Journal of the Atmospheric Sciences*, 63(5), 1498–1511. <https://doi.org/10.1175/jas3695.1>
- Danabasoglu, G., Lamarque, J.-F., Bacmeister, J., Bailey, D., DuVivier, A., Edwards, J., et al. (2020). The Community Earth System Model version 2 (CESM2). *Journal of Advances in Modeling Earth Systems*, 12(2), e2019MS001916. <https://doi.org/10.1029/2019ms001916>
- Donohoe, A., Frierson, D. M., & Battisti, D. S. (2014). The effect of ocean mixed layer depth on climate in slab ocean aquaplanet experiments [Journal Article]. *Climate Dynamics*, 43(3–4), 1041–1055. <https://doi.org/10.1007/s00382-013-1843-4>
- Emanuel, K. (2020). The relevance of theory for contemporary research in atmospheres, oceans, and climate. *AGU Advances*, 1(2), e2019AV000129. <https://doi.org/10.1029/2019av000129>
- Enderton, D., & Marshall, J. (2009). Explorations of atmosphere-ocean-ice climates on an aquaplanet and their meridional energy transports. *Journal of the Atmospheric Sciences*, 66(6), 1593–1611. <https://doi.org/10.1175/2008jas2680.1>
- Eyring, V., Bony, S., Meehl, G. A., Senior, C. A., Stevens, B., Stouffer, R. J., & Taylor, K. E. (2016). *Overview of the Coupled Model Intercomparison Project Phase 6 (CMIP6) experimental design and organization*, p. 9. Geoscientific Model Development (Online). (LLNL-JRNL-736881).
- Farneti, R., & Vallis, G. K. (2009). An Intermediate Complexity Climate Model (ICCMp1) based on the GFDL flexible modeling system. *Geoscientific Model Development*, 2(2), 73. <https://doi.org/10.5194/gmd-2-73-2009>
- Fasullo, J. T., & Trenberth, K. E. (2008). The annual cycle of the energy budget. Part II: Meridional structures and poleward transports. *Journal of Climate*, 21(10), 2313–2325. <https://doi.org/10.1175/2007jcli1936.1>
- Ferrari, R., Nadeau, L.-P., Marshall, D. P., Allison, L. C., & Johnson, H. L. (2017). A model of the ocean overturning circulation with two closed basins and a reentrant channel. *Journal of Physical Oceanography*, 47(12), 2887–2906. <https://doi.org/10.1175/jpo-d-16-0223.1>
- Ferreira, D., Marshall, J., & Campin, J.-M. (2010). Localization of deep water formation: Role of atmospheric moisture transport and geometrical constraints on ocean circulation. *Journal of Climate*, 23(6), 1456–1476. <https://doi.org/10.1175/2009jcli3197.1>
- Ferreira, D., Marshall, J., Ito, T., & McGee, D. (2018). Linking glacial-interglacial states to multiple equilibria of climate. *Geophysical Research Letters*, 45(17), 9160–9170. <https://doi.org/10.1029/2018gl077019>
- Frierson, D. M. W., Hwang, Y.-T., Fučkar, N. S., Seager, R., Kang, S. M., Donohoe, A., et al. (2013). Contribution of ocean overturning circulation to tropical rainfall peak in the Northern Hemisphere. *Nature Geoscience*, 6(11), 940–944. <https://doi.org/10.1038/ngeo1987>
- Gent, P. R., Willebrand, J., McDougall, T. J., & McWilliams, J. C. (1995). Parameterizing eddy-induced tracer transports in ocean circulation models. *Journal of Physical Oceanography*, 25(4), 463–474. [https://doi.org/10.1175/1520-0485\(1995\)025<0463:petti>2.0.co;2](https://doi.org/10.1175/1520-0485(1995)025<0463:petti>2.0.co;2)
- Gill, A. E. (1982). *Atmosphere—Ocean dynamics* [Book]. Elsevier.
- Griffies, S. M., Levy, M., Adcroft, A. J., Danabasoglu, G., Hallberg, R. W., Jacobsen, D., et al. (2015). Theory and numerics of the Community Ocean Vertical Mixing (CVMIX) project. *Technical Reports*.

- Grist, J. P., & Josey, S. A. (2003). Inverse analysis adjustment of the SOC air-sea flux climatology using ocean heat transport constraints. *Journal of Climate*, 16(20), 3274–3295. [https://doi.org/10.1175/1520-0442\(2003\)016<3274:iaots>2.0.co;2](https://doi.org/10.1175/1520-0442(2003)016<3274:iaots>2.0.co;2)
- Haarsma, R. J., Roberts, M. J., Vidale, P. L., Senior, C. A., Bellucci, A., Bao, Q., et al. (2016). High Resolution Model Intercomparison Project (HighResMIP v1.0) for CMIP6. *Geoscientific Model Development*, 9(11), 4185–4208. <https://doi.org/10.5194/gmd-9-4185-2016>
- Hack, J. J. (1994). Parameterization of moist convection in the National Center for Atmospheric Research community climate model (CCM2). *Journal of Geophysical Research*, 99(D3), 5551–5568. <https://doi.org/10.1029/93jd03478>
- Hall, A. (2004). The role of surface albedo feedback in climate. *Journal of Climate*, 17(7), 1550–1568. [https://doi.org/10.1175/1520-0442\(2004\)017<1550:tosaf>2.0.co;2](https://doi.org/10.1175/1520-0442(2004)017<1550:tosaf>2.0.co;2)
- Held, I. M. (2005). The gap between simulation and understanding in climate modeling. *Bulletin of the American Meteorological Society*, 86(11), 1609–1614. <https://doi.org/10.1175/bams-86-11-1609>
- Herrington, A. R., & Reed, K. A. (2017). An explanation for the sensitivity of the mean state of the community atmosphere model to horizontal resolution on aquaplanets. *Journal of Climate*, 30(13), 4781–4797. <https://doi.org/10.1175/jcli-d-16-0069.1>
- Hirt, C. W., Amsden, A. A., & Cook, J. L. (1974). An arbitrary Lagrangian-Eulerian computing method for all flow speeds. *Journal of Computational Physics*, 14(3), 227–253. [https://doi.org/10.1016/0021-9991\(74\)90051-5](https://doi.org/10.1016/0021-9991(74)90051-5)
- Holloway, G. (1997). Eddy transport of thickness and momentum in layer and level models. *Journal of Physical Oceanography*, 27(6), 1153–1157. [https://doi.org/10.1175/1520-0485\(1997\)027<1153:etotam>2.0.co;2](https://doi.org/10.1175/1520-0485(1997)027<1153:etotam>2.0.co;2)
- Holton, J. R., & Hakim, G. J. (2012). *An introduction to dynamic meteorology*. Academic Press.
- Holtslag, A. A. M., & Boville, B. A. (1993). Local versus nonlocal boundary-layer diffusion in a global climate model. *Journal of Climate*, 6(10), 1825–1842. [https://doi.org/10.1175/1520-0442\(1993\)006<1825:lvnbld>2.0.co;2](https://doi.org/10.1175/1520-0442(1993)006<1825:lvnbld>2.0.co;2)
- Hurrell, J. W., Holland, M. M., Gent, P. R., Ghan, S., Kay, J. E., Kushner, P. J., et al. (2013). The Community Earth System Model: A framework for collaborative research. *Bulletin of American Meteorological Society*, 94(9), 1339–1360. <https://doi.org/10.1175/bams-d-12-00121.1>
- Jansen, M. F., Adcroft, A., Khani, S., & Kong, H. (2019). Toward an energetically consistent, resolution aware parameterization of ocean mesoscale eddies. *Journal of Advances in Modeling Earth Systems*, 11(8), 2844–2860. <https://doi.org/10.1029/2019ms001750>
- Jansen, M. F., & Nadeau, L.-P. (2016). The effect of southern ocean surface buoyancy loss on the deep-ocean circulation and stratification. *Journal of Physical Oceanography*, 46(11), 3455–3470. <https://doi.org/10.1175/jpo-d-16-0084.1>
- Jeevanjee, N., Hassanzadeh, P., Hill, S., & Sheshadri, A. (2017). A perspective on climate model hierarchies. *Journal of Advances in Modeling Earth Systems*, 9(4), 1760–1771. <https://doi.org/10.1002/2017ms001038>
- Johnson, H. L., Cessi, P., Marshall, D. P., Schloesser, F., & Spall, M. A. (2019). Recent contributions of theory to our understanding of the Atlantic meridional overturning circulation. *Journal of Geophysical Research: Oceans*, 124(8), 5376–5399. <https://doi.org/10.1029/2019jc015330>
- Jones, C. S., & Cessi, P. (2016). Interbasin transport of the meridional overturning circulation. *Journal of Physical Oceanography*, 46(4), 1157–1169. <https://doi.org/10.1175/jpo-d-15-0197.1>
- Jones, C. S., & Cessi, P. (2017). Size matters: Another reason why the Atlantic is saltier than the Pacific. *Journal of Physical Oceanography*, 47(11), 2843–2859. <https://doi.org/10.1175/jpo-d-17-0075.1>
- Jones, C. S., & Cessi, P. (2018). Components of upper-ocean salt transport by the gyres and the meridional overturning circulation. *Journal of Physical Oceanography*, 48(10), 2445–2456. <https://doi.org/10.1175/jpo-d-18-0005.1>
- Kang, S. M., Held, I. M., Frierson, D. M. W., & Zhao, M. (2008). The response of the ITCZ to extratropical thermal forcing: Idealized slab-ocean experiments with a GCM. *Journal of Climate*, 21(14), 3521–3532. <https://doi.org/10.1175/2007jcli2146.1>
- Kaspi, Y., & Schneider, T. (2011). Downstream self-destruction of storm tracks. *Journal of the Atmospheric Sciences*, 68(10), 2459–2464. <https://doi.org/10.1175/jas-d-10-05002.1>
- Kessler, W. S. (2006). The circulation of the eastern tropical Pacific: A review. *Progress in Oceanography*, 69(2–4), 181–217. <https://doi.org/10.1016/j.pocean.2006.03.009>
- Large, W. G., McWilliams, J. C., & Doney, S. C. (1994). Oceanic vertical mixing: A review and a model with a nonlocal boundary layer parameterization. *Reviews of Geophysics*, 32(4), 363–403. <https://doi.org/10.1029/94rg01872>
- Lawrence, D. M., Fisher, R. A., Koven, C. D., Oleson, K. W., Swenson, S. C., Bonan, G., et al. (2019). The community land model version 5: Description of new features, benchmarking, and impact of forcing uncertainty. *Journal of Advances in Modeling Earth Systems*, 11(12).
- Li, H., & Srivastava, R. L. (2018). Impact of tropical cyclones on the global ocean: Results from multi-decadal global ocean simulations isolating tropical cyclone forcing [Journal Article]. *Journal of Climate*, 31(21).
- Lin, S.-J., & Rood, R. B. (1996). Multidimensional flux-form semi-Lagrangian transport schemes. *Monthly Weather Review*, 124(9), 2046–2070. [https://doi.org/10.1175/1520-0493\(1996\)124<2046:mffslt>2.0.co;2](https://doi.org/10.1175/1520-0493(1996)124<2046:mffslt>2.0.co;2)
- Lin, S.-J., & Rood, R. B. (1997). An explicit flux-form semi-Lagrangian shallow-water model on the sphere. *Quarterly Journal of the Royal Meteorological Society*, 123(544), 2477–2498. <https://doi.org/10.1002/qj.49712354416>
- Maher, P., Gerber, E. P., Medeiros, B., Merlis, T. M., Sherwood, S., Sheshadri, A., et al. (2019). Model hierarchies for understanding atmospheric circulation. *Review of Geophysics*, 57(2), 250–280. <https://doi.org/10.1029/2018rg000607>
- Manabe, S., & Bryan, K. (1969). Climate calculations with a combined ocean-atmosphere model. *Journal of the Atmospheric Sciences*, 26(4), 786–789. [https://doi.org/10.1175/1520-0469\(1969\)026<0786:ccwaco>2.0.co;2](https://doi.org/10.1175/1520-0469(1969)026<0786:ccwaco>2.0.co;2)
- Marshall, J., Ferreira, D., Campin, J.-M., & Enderton, D. (2007). Mean climate and variability of the atmosphere and ocean on an aquaplanet. *Journal of the Atmospheric Sciences*, 64(12), 4270–4286. <https://doi.org/10.1175/2007jas2226.1>
- Marshall, J., & Radko, T. (2003). Residual-mean solutions for the Antarctic circumpolar current and its associated overturning circulation. *Journal of Physical Oceanography*, 33(11), 2341–2354. [https://doi.org/10.1175/1520-0485\(2003\)033<2341:rsfac>2.0.co;2](https://doi.org/10.1175/1520-0485(2003)033<2341:rsfac>2.0.co;2)
- Medeiros, B., Williamson, D. L., & Olson, J. G. (2016). Reference aquaplanet climate in the Community Atmosphere Model, Version 5. *Journal of Advances in Modeling Earth Systems*, 8(1), 406–424. <https://doi.org/10.1002/2015ms000593>
- Molteni, F. (2003). Atmospheric simulations using a GCM with simplified physical parametrizations. I: Model climatology and variability in multi-decadal experiments. *Climate Dynamics*, 20(2–3), 175–191. <https://doi.org/10.1007/s00382-002-0268-2>
- Munk, W. H. (1966). Abyssal recipes. *Deep Sea Research and Oceanographic Abstracts*, 13(4), 707–730. [https://doi.org/10.1016/0011-7471\(66\)90602-4](https://doi.org/10.1016/0011-7471(66)90602-4)
- Munk, W., & Wunsch, C. (1998). Abyssal recipes II: Energetics of tidal and wind mixing. *Deep Sea Research I: Oceanographic Research Papers*, 45(12), 1977–2010. [https://doi.org/10.1016/s0967-0637\(98\)00070-3](https://doi.org/10.1016/s0967-0637(98)00070-3)
- Nadeau, L.-P., Ferrari, R., & Jansen, M. F. (2019). Antarctic sea ice control on the depth of North Atlantic deep water. *Journal of Climate*, 32(9), 2537–2551. <https://doi.org/10.1175/jcli-d-18-0519.1>
- Nadeau, L.-P., & Jansen, M. F. (2020). Overturning circulation pathways in a two-basin ocean model. *Journal of Physical Oceanography*, 50(8), 2105–2122. <https://doi.org/10.1175/jpo-d-20-0034.1>

- Neale, R. B., Chen, C.-C., Gettelman, A., Lauritzen, P. H., Park, S., Williamson, D. L. et al. (2010). Description of the NCAR Community Atmosphere Model (CAM 4.0). *NCAR Tech. Note NCAR/TN-486+STR*, 1(1), 1–12.
- Neale, R., & Hoskins, B. J. (2000). A standard test for AGCMs including their physical parametrizations: I: The proposal. *Atmospheric Science Letters*, 1(2), 101–107. <https://doi.org/10.1006/asle.2000.0019>
- Nilsson, J., Langen, P. L., Ferreira, D., & Marshall, J. (2013). Ocean basin geometry and the salinification of the Atlantic ocean. *Journal of Climate*, 26(16), 6163–6184. <https://doi.org/10.1175/jcli-d-12-00358.1>
- Pendergrass, A. G., & Hartmann, D. L. (2014). The atmospheric energy constraint on global-mean precipitation change. *Journal of Climate*, 27(2), 757–768. <https://doi.org/10.1175/jcli-d-13-00163.1>
- Polvani, L., Clement, A., Medeiros, B., Benedict, J., & Simpson, I. (2017). When less is more: Opening the door to simpler climate models, Eos, 98. Eos. *Transactions - American Geophysical Union*, 99(3), 15–16.
- Redi, M. H. (1982). Oceanic isopycnal mixing by coordinate rotation. *Journal of Physical Oceanography*, 12(10), 1154–1158. [https://doi.org/10.1175/1520-0485\(1982\)012<1154:ombr>2.0.co;2](https://doi.org/10.1175/1520-0485(1982)012<1154:ombr>2.0.co;2)
- Reed, K. A., & Jablonowski, C. (2012). Idealized tropical cyclone simulations of intermediate complexity: A test case for AGCMs. *Journal of Advances in Modeling Earth Systems*, 4(2). <https://doi.org/10.1029/2011ms000099>
- Schneider, T., Bischoff, T., & Haug, G. H. (2014). Migrations and dynamics of the intertropical convergence zone. *Nature*, 513(7516), 45–53. <https://doi.org/10.1038/nature13636>
- Schlitz, D. M., Fairman, J. G., Jr, Anderson, S., & Gardner, S. (2017). Build your own earth: A web-based tool for exploring climate model output in teaching and research. *Bulletin of the American Meteorological Society*, 98(8), 1617–1623. <https://doi.org/10.1175/bams-d-16-0121.1>
- Scoccimarro, E., Fogli, P. G., Reed, K. A., Gualdi, S., Masina, S., & Navarra, A. (2017). Tropical cyclone interaction with the ocean: The role of high-frequency (subdaily) coupled processes. *Journal of Climate*, 30(1), 145–162. <https://doi.org/10.1175/jcli-d-16-0292.1>
- Shao, A. E., Adcroft, A., Hallberg, R., & Griffies, S. M. (2020). A general-coordinate, nonlocal neutral diffusion operator. *Journal of Advances in Modeling Earth Systems*, 12(12), e2019MS001992. <https://doi.org/10.1029/2019ms001992>
- Smith, R. S., Dubois, C., & Marotzke, J. (2006). Global climate and ocean circulation on an aquaplanet ocean-atmosphere general circulation model. *Journal of Climate*, 19(18), 4719–4737. <https://doi.org/10.1175/jcli3874.1>
- Solomon, H. (1971). On the representation of isentropic mixing in ocean circulation models. *Journal of Physical Oceanography*, 1(3), 233–234. [https://doi.org/10.1175/1520-0485\(1971\)001<233:otriom>2.0.co;2](https://doi.org/10.1175/1520-0485(1971)001<233:otriom>2.0.co;2)
- Stephens, G. L., O'Brien, D., Webster, P. J., Pilewski, P., Kato, S., & Li, J.-l. (2015). The albedo of earth. *Review of Geophysics*, 53(1), 141–163. <https://doi.org/10.1002/2014rg000449>
- Sun, Y., Li, L. Z., Ramstein, G., Zhou, T., Tan, N., Kageyama, M., & Wang, S. (2019). Regional meridional cells governing the interannual variability of the Hadley circulation in boreal winter. *Climate Dynamics*, 52(1–2), 831–853. <https://doi.org/10.1007/s00382-018-4263-7>
- Tabor, C. R., Feng, R., & Otto-Bliesner, B. L. (2019). Climate responses to the splitting of a supercontinent: Implications for the breakup of pangea. *Geophysical Research Letters*, 46(11), 6059–6068. <https://doi.org/10.1029/2018gl081510>
- Talley, L. D. (2011). *Descriptive physical oceanography: An introduction*. Academic press.
- Vallis, G. K. (2017). *Atmospheric and oceanic fluid dynamics*. Cambridge University Press.
- Vallis, G. K., & Farneti, R. (2009). Meridional energy transport in the coupled atmosphere-ocean system: Scaling and numerical experiments. *Quarterly Journal of the Royal Meteorological Society*, 135(644), 1643–1660. <https://doi.org/10.1002/qj.498>
- Voigt, A., & Shaw, T. A. (2015). Circulation response to warming shaped by radiative changes of clouds and water vapor. *Nature Geoscience*, 8(2), 102–106. <https://doi.org/10.1038/ngeo2345>
- Watanabe, M. (2008a). Two regimes of the equatorial warm pool. Part I: A simple tropical climate model. *Journal of Climate*, 21(14), 3533–3544. <https://doi.org/10.1175/2007jcli2151.1>
- Watanabe, M. (2008b). Two regimes of the equatorial warm pool. Part II: Hybrid coupled GCM experiments. *Journal of Climate*, 21(14), 3545–3560. <https://doi.org/10.1175/2007jcli2152.1>
- Wolfe, C. L., & Cessi, P. (2010). What sets the strength of the middepth stratification and overturning circulation in eddying ocean models? *Journal of Physical Oceanography*, 40(7), 1520–1538. <https://doi.org/10.1175/2010jpo4393.1>
- Wolfe, C. L., & Cessi, P. (2011). The adiabatic pole-to-pole overturning circulation. *Journal of Physical Oceanography*, 41(9), 1795–1810. <https://doi.org/10.1175/2011jpo4570.1>
- Wyrki, K. (1981). An estimate of equatorial upwelling in the pacific. *Journal of Physical Oceanography*, 11(9), 1205–1214. [https://doi.org/10.1175/1520-0485\(1981\)011<1205:aeoeui>2.0.co;2](https://doi.org/10.1175/1520-0485(1981)011<1205:aeoeui>2.0.co;2)
- Yang, B., Qian, Y., Lin, G., Leung, L. R., Rasch, P. J., Zhang, G. J., et al. (2013). Uncertainty quantification and parameter tuning in the cam5 Zhang-McFarlane convection scheme and impact of improved convection on the global circulation and climate. *Journal of Geophysical Research - D: Atmospheres*, 118(2), 395–415. <https://doi.org/10.1029/2012jd018213>
- Zhang, G. J., & McFarlane, N. A. (1995). Sensitivity of climate simulations to the parameterization of cumulus convection in the Canadian climate center general circulation model. *Atmosphere-Ocean*, 33(3), 407–446. <https://doi.org/10.1080/07055900.1995.9649539>
- Zhang, H., Clement, A., & Medeiros, B. (2016). The meridional mode in an idealized aquaplanet model: Dependence on the mean state. *Journal of Climate*, 29(8), 2889–2905. <https://doi.org/10.1175/jcli-d-15-0399.1>